

ANDREW R. MCCLUSKEY
for the degree of DOCTOR OF PHILOSOPHY

COARSE-GRAINED
MODELLING FOR
SOFT MATTER
SCATTERING

UNIVERSITY OF BATH
DEPARTMENT OF CHEMISTRY

DIAMOND LIGHT SOURCE

Copyright © 2019 Andrew R. McCluskey

Attention is drawn to the fact that copyright of this thesis rests with the author. A copy of this thesis has been supplied on condition that anyone who consults it is understood to recognise that its copyright rests with the author and that they must not copy it or use material from it except as permitted by law or with the consent of the author.

This work is licensed under a Creative Commons "Attribution 4.0 International" license.



First printing, April 2019

“ATTICUS TOLD ME TO DELETE THE ADJECTIVES AND I’D HAVE THE FACTS.”

Scout Finch – To Kill a Mockingbird

DECLARATION OF AUTHORSHIP

I, Andrew R. McCluskey, declare that this thesis titled “Coarse-grained modelling for soft matter scattering” and the work presented in it are my own. I confirm that:

- where the thesis or any part of the thesis such as a published paper, has been produced jointly with others, that a substantial part is the original work of myself, and
- where the thesis incorporates material already submitted for another degree, the extent of that material and the degree, if any, obtained.

Signed:

Date:

PUBLICATIONS

Some of the information in Chapter 2 has been previously published in:

- A. R. McCluskey *et al.* *Curr. Org. Chem.* 22.8 (2018), pp. 750–757.

Some of the work covered in Chapter ?? has been previously published in:

- A. R. McCluskey *et al.* *Phys. Chem. Chem. Phys.* 21.11 (2019), pp. 6133–6141.

Some of the work covered in Chapter ?? has been previously published in:

- A. R. McCluskey *et al.* *J. Phys. Comm.* Accepted (2019).

Some of the work covered in Chapter ?? has been previously published in:

- A. R. McCluskey *et al.* *J. Open Source Educ.* 1.2 (2018), pp.19–21.
- A. R. McCluskey *et al.* *J. Appl. Crystallogr.* Accepted (2019).

REPRODUCIBILITY STATEMENT

This thesis exists as a piece of completely reproducible research. I have endeavoured to include as much algorithmic and methodological detail within the text, and where relevant working Code Blocks written in Python, and including appropriate documentation strings in the NumPy format, have been included for clarity.

However, in order to provide complete, and easy, reproducibility an electronic supplementary information (ESI) is available online in the form of a Git repository. This ESI provides full details of the analyses performed in this work and access to an automated analysis workflow.

The ESI may be accessed at the following doi:[10.5281/zenodo.xxxxxxx](https://doi.org/10.5281/zenodo.xxxxxxx).

ACKNOWLEDGEMENTS

This is where I will acknowledge people. Need to remember everyone...

CONTENTS

<i>1</i>	<i>Introduction</i>	<i>1</i>
1.1	<i>Soft matter self-assembly</i>	<i>1</i>
1.2	<i>Analysis of soft matter scattering</i>	<i>3</i>
1.3	<i>Coarse-graining of soft matter systems</i>	<i>4</i>
1.4	<i>Optimisation methodologies</i>	<i>5</i>
1.5	<i>Educational materials</i>	<i>5</i>
<i>2</i>	<i>Theory</i>	<i>7</i>
2.1	<i>Probing radiation</i>	<i>7</i>
2.2	<i>Scattering</i>	<i>11</i>
2.3	<i>Classical simulation</i>	<i>28</i>
2.4	<i>Optimisation & sampling methods</i>	<i>33</i>
<i>A</i>	<i>Additional Code Blocks for Differential Evolution</i>	<i>45</i>

LIST OF FIGURES

- 1.1 Three examples of soft matter species; (a) a 43 C₁₀TAB surfactant micelle, reprinted with permission from R. Hargreaves *et al.* *J. Am. Chem. Soc.* 133.41 (2011), pp. 16524–16536, copyright 2011 American Chemical Society, (b) the tunable interactions of colloids, reprinted with permission from D. J. Kraft *et al.* *J. Phys. Chem. B* 115.22 (2011), pp. 7175–7181, copyright 2011 American Chemical Society, and (c) generated using VMD (W. Humphrey *et al.* *J. Mol. Graph.* 14.1 (1996), pp. 33–38) from the crystal structure of T4-lysozyme D. R. Rose *et al.* *Protein Eng. Des. Sel.* 2.4 (1988), pp. 277–282. 1
- 1.2 A graphical representation of the packing parameters and information of the resulting self-assembled structure. 3
- 1.3 Potential energy surfaces for an all-atom vs a coarse-grained potential model, reprinted with permission of the American Chemical Society from S. Kmiecik *et al.* *Chem. Rev.* 116.14 (2016), pp. 7898–7936. 5
- 2.1 A schematic representation of a synchrotron radiation source, identifying the Linac, the booster ring, the radio-frequency cavities (rf), the bending magnet (BM) and the insertion device (ID). Reprinted, with permission of Springer Nature Customer Service Centre GmbH: Springer Nature, from M. C. Garcia-Gutierrez *et al.* “Bases of Synchrotron Radiation, Light Sources, and Features of X-Ray Scattering Beamlines”. In: *Applications of Synchrotron Light to Scattering and Diffraction in Materials and Life Sciences*. 2009, pp. 1–22. 8
- 2.2 A diagram of an undulator insertion device, such as that on I07 and I22, where λ_P is the period length between opposing magnets. Reprinted, with permission of Springer Nature Customer Service Centre GmbH: Springer Nature, from M. C. Garcia-Gutierrez *et al.* “Bases of Synchrotron Radiation, Light Sources, and Features of X-Ray Scattering Beamlines”. In: *Applications of Synchrotron Light to Scattering and Diffraction in Materials and Life Sciences*. 2009, pp. 1–22. 9
- 2.3 A representation of how different techniques can be used to probe various length scales. Reprinted, with permission of Oxford University Press, from D. S. Sivia. *Elementary Scattering Theory: For X-Ray and Neutron Users*. 2011. 11

- 2.4 A schematic of the scattering of some probing radiation by a sample (blue circle). Adapted, with permission of Oxford University Press, from D. S. Sivia. *Elementary Scattering Theory: For X-Ray and Neutron Users*. 2011. 12
- 2.5 A vector diagram describing an elastic scattering event, where \mathbf{k}_i is the incident wavevector, \mathbf{k}_f is the final wavevector, 2θ is the scattering angle, and \mathbf{q} is the scattering vector. Adapted, with permission of Oxford University Press, from D. S. Sivia. *Elementary Scattering Theory: For X-Ray and Neutron Users*. 2011. 12
- 2.6 A schematic showing the propagation of the wave of probing radiation (green lines) radially outwards following the scattering event, where r is the magnitude of the displacement vector. Adapted, with permission of Oxford University Press, from D. S. Sivia. *Elementary Scattering Theory: For X-Ray and Neutron Users*. 2011. 13
- 2.7 A schematic showing the interaction of radiation scattered by two particles that are separated by the vector \mathbf{R}_j . Adapted, with permission of Oxford University Press, from D. S. Sivia. *Elementary Scattering Theory: For X-Ray and Neutron Users*. 2011. 14
- 2.8 A schematic showing the geometry of a typical specular reflectometry experiment from a layered sample. Reprinted, with permission of Oxford University Press, from D. S. Sivia. *Elementary Scattering Theory: For X-Ray and Neutron Users*. 2011. 16
- 2.9 A graphical representation of the kinematic approach; (a) the Heaviside function describing the scattering length density profile of a bare silicon substrate, (b) the δ -function arising from the first derivative of the function in (a), and (c) the reflectometry profile resulting from the kinematic approach, where the orange line at $R = 1$ identifies the break down between experimental and theory in the kinematic approach. Adapted, with permission of Oxford University Press, from D. S. Sivia. *Elementary Scattering Theory: For X-Ray and Neutron Users*. 2011. 18
- 2.10 A schematic diagram showing the reflected (r) and transmitted (t) waves when an incident (i) wave enters an interface of thickness d , where the refractive indices of each layer are n_0 , n_1 , and n_2 . Adapted, with permission of Elsevier, from F. Foglia *et al.* *Curr. Opin. Colloid Interface Sci.* 20.4 (2015), pp. 235–243. 19
- 2.11 A comparison of the kinematic approach (blue solid line), and the dynamical approach (green dashed line), to determine the reflected intensity from the material with the scattering length density profile given in Figure 2.9(a). It is clear that at low q , there is a noticeable deviation between the two. 21
- 2.12 The effect of a Fourier transform (a) the scattering length density profile for some object with a width of 10 \AA , (b) the Fourier transform of this object showing the minima in the differential cross section at values of $2n\pi/10$, where n is some integer. 21

- 2.13 A schematic of the D22 instrument of the ILL. Reprinted with permission of Springer Nature Customer Service Centre GmbH: Springer Nature from I. Grillo. "Small-Angle Neutron Scattering and Applications in Soft Condensed Matter". In: *Soft-Matter Characterization*. 2008, pp. 723–782. 21
- 2.14 The Guinier plot, (a) the ideal scattering profile from a sphere of radius 20 Å, (b) the associated Guinier plot, with a straight line (orange) at low- q showing the radius of gyration to be ~ 15.5 Å. 23
- 2.15 The SANS profile of a micelle of C₁₆TAB with radius (50 ± 3) Å (circles, generated using SASView *SASview for Small Angle Scattering*. URL: <http://www.sasview.org> (Accessed 2016-10-26), with instrumental smearing) compared with a curve of Equation 2.42, where $R = 50$ Å (solid line). 24
- 2.16 The variation of the average neutron scattering length, $\langle b \rangle$ (circles), with atomic mass, μ . The standard deviation, Δb , is indicated with the shaded regions. Reproduced, with permission of Oxford University Press, from D. S. Sivia. *Elementary Scattering Theory: For X-Ray and Neutron Users*. 2011. 26
- 2.17 The effect of varying the scattering length density of the solvent in a micelle system, (a) the system in a pure solvent, (b) the solvent is contrast matched to the surfactant tails, and (c) the solvent is contrast matched to the surfactant heads. 27
- 2.18 The form of each component; attractive (blue), repulsive (orange), of the Lennard-Jones potential model (green) for argon, using parameters in A. Rahman. *Phys. Rev.* 136 (2A 1964), A405–A411. 30
- 2.19 A graphical representation of the periodic boundary conditions. Reprinted, with permission of Elsevier, from D. Frenkel *et al.* *Understanding Molecular Simulation: From Algorithms to Applications*. 1996. 30
- 2.20 Three examples of the MARTINI coarse-graining mechanism for (a) aspartic acid, (b) a water cluster, and (c) a molecule of DPPC. Reprinted with permission of the Institute of Physics, from K. Pluhackova *et al.* *J. Phys. Condens. Matter* 27.32 (2015), p. 323103. 33
- 2.21 An example of a differential evolution (DE) algorithm as applied to an Ackley function, where $a = 20$, $b = 0.2$, and $c = 2\pi$. The mutation and recombination constant in this implementation are both 0.5. Each different coloured line represents a different candidate solution. The optimisation was stopped after 100 iterations had run. 35
- 2.22 An example of a particle swarm optimisation as applied to an Ackley function, where $a = 20$, $b = 0.2$, and $c = 2\pi$. For the particle swarm, the following parameters were used $\omega = 0.9$, $\psi_g = 0.05$, and $\psi_p = 0.05$. Each different coloured line represents a different candidate solution. The optimisation was stopped after 100 iterations had run. 38

2.23 An example of a four variable (two nearby Gaussian functions of different sizes with added random noise and some fractional uncertainty) problem probed using a MCMC method, using values of $a = 0.1$, θ_1 and θ_2 correspond to the integral of the Gaussian function, while θ_3 and θ_4 indicate their positions; (a)-(d) histograms of the probability distribution function for each of the variables, and (e) the data (blue circles), the optimised solution (orange line), and a series of probable solutions (green lines) showing the variability present in the data uncertainty. 39

LIST OF TABLES

- 2.1 A comparison of the photon brilliance from different light sources. Adapted, with permission of Oxford University Press, from D. S. Sivia. *Elementary Scattering Theory: For X-Ray and Neutron Users*. 2011. 9
- 2.2 Examples of coherent and incoherent scattering cross-sections. Reproduced, with permission from Elsevier, from P. Schurtenberger. "Contrast and Contrast Variation in Neutron, x-Ray and Light Scattering". In: *Neutron, X-Rays and Light. Scattering Methods Applied to Soft Condensed Matter*. 2002, pp. 145–170. 27

LIST OF CODE BLOCKS

2.1	An example Python code block for the Abelès method for the calculation of reflectometry, adapted from A. R. J. Nelson <i>et al.</i> <i>J. Appl. Crystallogr.</i> 52.1 (2019), pp. 193–200.	20
	reports/code_blocks/reflectometry.py	20
	reports/code_blocks/lennardjones.py	31
2.2	Code that may be used to generate the Lennard-Jones energy for a given atomistic system, which accounts for the periodic boundary condition and the energy cut-off distance.	31
	reports/code_blocks/diff_evo.py	36
2.3	An example of a simple implementation for a DE algo- rithm as described in M. Björck. <i>J. Appl. Crystallogr.</i> 44.6 (2011), pp. 1198–1204.	36
	reports/code_blocks/part_swarm.py	38
2.4	An example of the particle swarm optimisation algorithm from R. Poli. <i>J. Artif. Evol. Appl.</i> 2008 (2008), pp. 1–10.	38
2.5	An example of the Metropolis-Hastings MCMC algorithm N. Metropolis <i>et al.</i> <i>J. Chem. Phys.</i> 21.6 (1953), pp. 1087– 1092; W. K. Hastings. <i>Biometrika</i> 57.1 (1970), pp. 97–109.	40
	reports/code_blocks/mutation.py	45
A.1	The mutation step used in a classical trial method for a differential evolution algorithm, as described in Björck, “Fitting with Differential Evolution: An Introduction and Evaluation”, op. cit.	45
	reports/code_blocks/recombination.py	45
A.2	The recombination step used in a classical trial method for a differential evolution algorithm, as described in <i>ibid.</i>	45
	reports/code_blocks/selection.py	46
A.3	The selection step used in a differential evolution algo- rithm, as described in <i>ibid.</i>	46

LIST OF ABBREVIATIONS

ACMW	air-contrast matched water
APM	area per molecule
cmc	critical micelle concentration
C₁₀TA⁺	<i>n</i> -decyltrimethylammonium
C₁₀TAB	<i>n</i> -decyltrimethylammonium bromide
C₁₆TAB	<i>n</i> -hexadecyltrimethylammonium bromide
CCP-SAS	collaborative computational project for small angle scattering
CPU	central processing unit
DDM	<i>n</i> -dodecyl- β - <i>D</i> -maltoside
DE	differential evolution
DES	deep eutectic solvent
DLS	Diamond Light Source
DM	<i>n</i> -decyl- β - <i>D</i> -maltoside
DMSO	dimethyl sulfoxide
DLPC	1,2-dilauroyl- <i>sn</i> -glycero-3-phosphocholine
DMPC	1,2-dimyristoyl- <i>sn</i> -glycero-3-phosphocholine
DMPG	1,2-dimyristoyl- <i>sn</i> -glycero-3-phospho-(1'-rac-glycerol)
DSPC	1,2-distearoyl- <i>sn</i> -glycero-3-phosphocholine
DPPC	1,2-dipalmitoyl- <i>sn</i> -glycero-3-phosphocholine
DPC	dodecylphosphocholine
DPD	dissipative particle dynamics
DVTD	differential vibrating tube densimetry
ESI	electronic supplementary information
ESRF	European Synchrotron Radiation Facility
ESS	European Spallation Source
GIXD	grazing-incidence X-ray diffraction
GPU	graphical processing units
hdDES	partially deuterated deep eutectic solvent
hDES	hydrogenated deep eutectic solvent
ILL	Institut Laue-Langevin
LC	Liquid-Condensed
LE	Liquid-Expanded
MCMC	Markov chain Monte Carlo
MD	molecular dynamics
MPI	message passing interface
NB	neutral buoyancy
NPT	constant number, pressure, and temperature

NR	neutron reflectometry
NVE	constant number, volume, and energy
NVT	constant number, volume, and temperature
OER	open education resource
PBC	periodic boundary condition
PC	phosphocholine
PDF	probability distribution function
PFTE	polytetrafluoroethylene
PG	phosphatidylglycerol
PME	particle mesh Ewald
PSO	particle swarm optimisation
RDF	radial distribution function
SANS	small angle neutron scattering
SAS	small angle scattering
SDS	sodium dodecyl sulfate
SLD	scattering length density
SAXS	small angle X-ray scattering
SPC	single point charge
STFC	Science & Technology Facilities Council
ToF	time-of-flight
VMD	visual molecular dynamics
wph	water molecules per head group
WAXS	wide angle X-ray scattering
XRR	X-ray reflectometry

PHYSICAL CONSTANTS

	$\pi = 3.1415 \dots$
Planck constant	$h = 6.626 \dots \times 10^{-34} \text{ J s}$
Golden ratio	$\Phi = 1.618 \dots$
dielectric permittivity of the vacuum	$\epsilon_0 = 8.854 \dots \times 10^{-12} \text{ F m}^{-1}$
charge of electron	$e = 1.602 \dots \times 10^{-19} \text{ C}$
Boltzmann constant	$k_B = 1.381 \dots \times 10^{-23} \text{ J K}^{-1}$

LIST OF SYMBOLS

a	step size	
a_0	optimum head-group area	m^2
b	scattering length	m
b	bond length	m
b_i	best candidate solution	
b_0	equilibrium bond length	m
d_h	phospholipid head layer thickness	m
d_t	phospholipid tail layer thickness	m
d_x	length of object	m
k_m	mutation constant	
l_0	length of hydrophobic tail	m
m	mass	kg
n	number of scattering vectors	
n_i	refractive index	
p	packing parameter	
p	parallel component	
q	scattering magnitude	m^{-1}
$q_{i,j}$	electronic charge	
r	displacement vector magnitude	m^{-1}
$r_{n,n+1}$	Fresnel equation coefficient	
s	serial component	
t	time	s
t_F	time-of-flight	s
$A_{1,2,3}$	dihedral constants	J
B	resultant matrix	
E_{bonded}	bonded energy	J
E_k	kinetic energy	J
$E_{\text{non-bonded}}$	non-bonded energy	J
E_{total}	total energy	J
F	some function	
I	intensity	
K_b	bond force constant	J m^{-2}
K_θ	angle force constant	J rad^{-2}
L_F	length-of-flight	m
M_n	layer matrix	
N	number of some item	
N_P	number of magnets	

N_ρ	number density	
$P(q)$	form factor	
R	reflected intensity	
$R_{1,2}$	some random number	
R_g	radius of gyration	m
R_i	incidence rate	s ⁻¹
R_s	radius of sphere	m
S	surface area	m ²
$S(q)$	structure factor	
T	temperature	K
U	uniform distribution	
V	volume	m ³
V_c	volume of hydrophobic tail	m ³
V_h	phospholipid head volume	m ³
V_n	volume of layer	m ³
V_p	volume of particle	m ³
V_t	phospholipid tail volume	m ³
a	acceleration	m s ⁻²
f	force	N
g	global best	
k_i	incident wavevector	m ⁻¹
k_f	final wavevector	m ⁻¹
m	mutant vector	
o	offspring population	
p	parent population	
q	scattering wavevector	m ⁻¹
r	displacement	m
s	personal best	
v	velocity	m s ⁻¹
x	position	m
R	particle position	m
β_c	fraction of the speed of light	
β_n	phase factor	
δ	infinitesimally small change	
ε	depth of potential well	J
ζ	figure of merit	
2θ	scattering angle	rad
θ	angle	rad
θ	some solution	
θ_0	equilibrium angle	rad
θ_c	critical angle	rad
θ_e	angle between electron and photon	rad
λ	wavelength	m
π	surface pressure	mN m ⁻¹
σ	distance at zero	m
σ_{coh}	coherent scattering cross-section	m
σ_{incoh}	incoherent scattering cross-section	m
$\sigma_{n,n+1}$	interfacial roughness	m

ϕ	scattering angle	
ϕ	dihedral angle	rad
ϕ_g	global acceleration coefficient	
ϕ_i	volume fraction of solvation	
ϕ_p	personal acceleration coefficient	
χ^2	a figure of merit	
ψ_0	wave at point 0	
ψ_i	wave at point i	
ψ_f	final scattered wave	
ω	frequency	s^{-1}
ω	initial weight	
ω_i	incident frequency	s^{-1}
ω_f	final frequency	s^{-1}
Δt	timestep	s
Θ	new solution	
Φ	incident flux	
$d\sigma(q)/d\Omega$	differential cross-section	

ABSTRACT

This work uses different coarse-graining methodologies to assist in the analysis of scattering measurements from soft matter species, such as surfactant monolayers and micelles. The term ‘coarse-graining’ is used broadly in this work; to describe the coarse-graining of a classical simulation potential model, a surfactant monolayer model that consists two layers, and a severe coarse-graining methodology that describes a surfactant molecule as just a position and direction in space. In all three cases, the aim of the applied coarse-graining is to improve the methods of analysis that may be performed in the analysis of reflectometry and small angle scattering measurements.

A surfactant monolayer model, that was considerate of the chemical bond between the surfactant heads and tails, was developed for the analysis of reflectometry measurements from a phospholipid monolayer at the interface between air and a deep eutectic solvent. This model allowed for a unique insight into the structure of the monolayer at the given interface. To assess the utility of coarse-grained potential models in the analysis of neutron reflectometry, a phospholipid monolayer was simulated using three different potential models, of different particle grain-size. This allowed for a better understanding of the simulation resolution necessary to accurately and successfully apply simulation-driven analysis to reflectometry. Finally, a severely coarse-grained description of a surfactant was used in a particle swarm optimisation to try and develop a starting structure for a multiple micelle simulation, where the experimental scattering profile was the optimisation target.

Alongside the development and application of coarse-graining methodologies, the final chapter of this work describes the development of open-source software and teaching materials for the introduction of classical molecular simulation. These educational resources introduce scattering users to simulation and its utility in scattering analysis, to enable a future where simulation driven analysis may be performed accurately by all.

1

INTRODUCTION

Soft matter is an umbrella term for many different types of material. These include micelles; sub-micron sized, dynamic agglomerates of amphiphilic molecules such as surfactants or block copolymers, colloidal solutions; where the interaction between the colloids may be controlled through chemical modification, or proteins; where the polar nature of different amino acids leads to the protein folding into a highly organised, and biologically relevant, shape. Some examples of these soft matter systems are shown in Figure 1.1. These species, initially, appear rather disparate, however, there are a few important commonalities among soft matter systems:¹

- the lengths scales are intermediate between atomistic and macroscopic,²
- for soft matter systems the energy of a structural distortion is similar to thermal energy, so the material is in constant flux,
- this thermal motion can lead to the formation of complex, hierarchical structures due to the balance between enthalpy and entropy, this process is referred to as self-assembly.

¹ R. A. L. Jones. *Soft Condensed Matter*. 2002.

² typically 1×10^{-8} – 1×10^{-5} m.

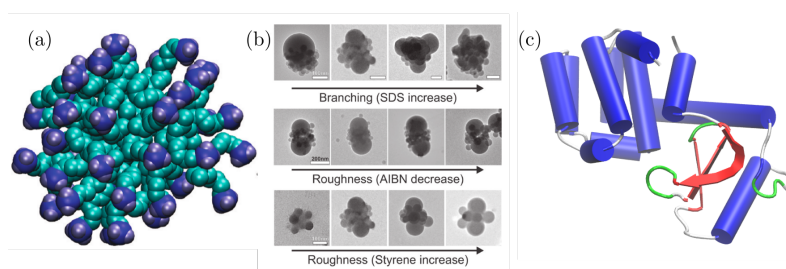


Figure 1.1: Three examples of soft matter species; (a) a 43 C₁₀ TAB surfactant micelle, reprinted with permission from R. Hargreaves *et al. J. Am. Chem. Soc.* 133.41 (2011), pp. 16524–16536, copyright 2011 American Chemical Society, (b) the tunable interactions of colloids, reprinted with permission from D. J. Kraft *et al. J. Phys. Chem. B* 115.22 (2011), pp. 7175–7181, copyright 2011 American Chemical Society, and (c) generated using VMD (W. Humphrey *et al. J. Mol. Graph.* 14.1 (1996), pp. 33–38) from the crystal structure of T4-lysozyme D. R. Rose *et al. Protein Eng. Des. Sel.* 2.4 (1988), pp. 277–282.

1.1 SOFT MATTER SELF-ASSEMBLY

Soft matter self-assembly is the ability for soft matter systems to form organised structures in solution. These are of particular interest industrially, where surfactant and polymer self-assembly play

³ L. L. Schramm *et al.* *Annu. Rep. Prog. Chem., Sect. C: Phys. Chem.* 99 (2003), pp. 3–48.

⁴ K. Simons *et al.* *Nat. Rev. Mol. Cell Biol.* 1 (2000), pp. 31–39.

⁵ J. Israelachvili. *Intermolecular and Surface Forces*. 2011.

⁶ D. Schmaljohann. *Adv. Drug Deliv. Rev.* 58.15 (2006), pp. 1655–1670; M. Sammalkorpi *et al.* *J. Phys. Chem. B* 113.17 (2009), pp. 5863–5870.

⁷ M. J. Rosen *et al.* *Surfactants and Interfacial Phenomena*. 2012.

⁸ J. Goodwin. *Colloids and Interfaces with Surfactants and Polymers*. 2009.

⁹ Ibid.

¹⁰ The lowest temperature at which agglomerates will form.

¹¹ D. Jurašin *et al.* *Soft Matter* 9.12 (2013), p. 3349; F. Cordobés *et al.* *J. Colloid Interface Sci.* 187.2 (1997), pp. 401–417.

¹² Israelachvili, *Intermolecular and Surface Forces*, op. cit.

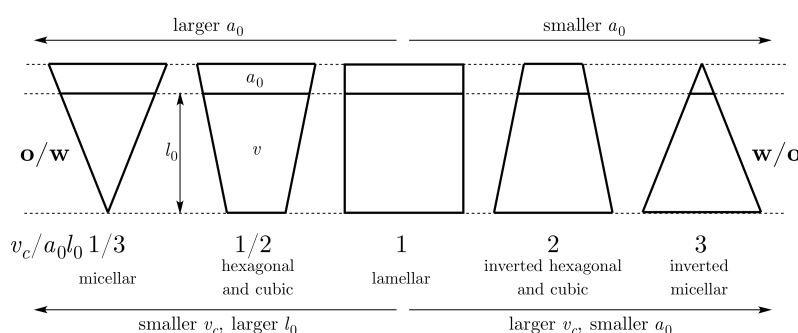
an import role in food, commodity, and speciality chemicals.³ Self-assembly processes are important from a biological perspective as it is phospholipids, a family of surface-active biomolecules, which make up the bilayers that protect cells.⁴ The structures that result from the self-assembly of soft matter species have fluid-like properties. This is due to the fact that the subunits are held together by weak forces such as the van der Waals, hydrophobic, hydrogen-bonding, and screen electrostatic interactions.⁵ This means that the structure of a self-assembled species is susceptible to changes in the local chemical environment, such as pH or salt concentration.⁶

The focus of this work is on the self-assembly of surfactant molecules. Surfactant is a general term for any molecule which is “surface-active”, to say that they will interact at an interface.⁷ Surfactants are generally made up of two components; one part is highly soluble in one of the interfacial phases, while the other is not.⁸ Usually, surfactants consist of a hydrocarbon tail, which is hydrophobic, and some hydrophilic head group, which can be ionic or non-ionic. When surfactants are present in water, the two components will interact differently with the solvent. A hydration sphere of water molecules will form around the hydrophilic head group, effectively allowing the head group to take part in the water’s hydrogen-bonding network. Whereas, the lyophilic tail has a structure-breaking effect on the hydrogen bonding network, termed the “hydrophobic effect”. The free energy deficit of this structure-breaking can be reduced through the aggregation of these hydrophobic groups, as the van der Waals attraction between tail groups is larger than that present between tail groups and water molecules. There is a decrease in entropy from the tail organisation, however, this is offset by the entropic increase from the water structure breakup. Finally, by considering the effect of the, often charged, head groups being close together, it is thought that the majority of the charge can be screened by the presence of a counter-ion, or water molecules, bound to the head group.⁹ This means that at low concentrations, where it is statistically unlikely for an agglomerate to form, the majority of surfactants will sit at the air-water interface, as the concentration is increased, assuming the system is above the Krafft temperature,¹⁰ organised structures will begin to appear.

The structures can be formed from surfactant solutions are diverse; featuring micellar, hexagonal, cubic, and lamellar mesophases. These mesophases have a significant impact on the macroscopic properties of the system, for example the liquid crystalline hexagonal phase can present interesting viscoelastic behaviour.¹¹ The mesophase that is formed is dependent on the shape of the underlying surfactants, Israelachvili described this dependency in terms of the dimensionless surfactant packing parameter, p .¹²

$$p = \frac{V_c}{a_0 l_0}, \quad (1.1)$$

where, V_c is the volume of the hydrophobic tail, l_0 is the length of the tail, and a_0 is the optimum head group area. This parameter can be used to estimate the geometry of the resulting self-assembled structure, detailed in Figure 1.2. It is important to note that the optimum head group area accounts for the hydration sphere of the head group. A short tail surfactant, such as *n*-decyltrimethylammonium bromide,¹³ will have a very small packing parameter resulting in small spherical micelles. Whereas, the twin-tailed phospholipids, such as 1,2-dipalmitoyl-*sn*-glycero-3-phosphocholine,¹⁴ will have a much larger packing parameter due to the larger tail volume and length, therefore this surfactant will form a lamellar bilayer in solution.



¹³ Commonly abbreviated to C₁₀TAB.

¹⁴ Known as DPPC.

Figure 1.2: A graphical representation of the packing parameters and information of the resulting self-assembled structure.

This work will focus on the investigation of surfactant monolayers and micellar systems. These represent interesting model systems of significant interest both technologically¹⁵ and biologically.¹⁶ Both of these systems are regularly investigated using X-ray and neutron elastic scattering techniques, with analysis performed in a model-dependent fashion.¹⁷

1.2 ANALYSIS OF SOFT MATTER SCATTERING

The use of neutron and X-ray scattering experiments for the study of soft matter is well developed, with early research into the structure of phospholipid monolayers by reflectometry methods being conducted in the late 1970s by Albrecht *et al.*¹⁸ While, the work of Kratky and Porod,¹⁹ who used small angle X-ray scattering for the study of colloidal systems was published in 1949. Since these early works, instrumentation developments have enabled more challenging experiments to be conducted, such as time-resolved studies²⁰ and the study of floating lipid bilayers.²¹

However, the analysis of soft matter scattering has changed little since these early works, still typically involving the use of very coarse models. These include the shape-based modelling common in small angle scattering²² and reflectometry analysis.²³ More sophisticated model refinements have been developed, such as the use of Monte-Carlo sampling,²⁴ differential evolution op-

¹⁵ N. Anton *et al.* *Int. J. Pharm.* 398.1-2 (2010), pp. 204–209; M. Zagnoni. *Lab on a Chip* 12.6 (2012), p. 1026.

¹⁶ K. Kataoka *et al.* *Adv. Drug Deliv. Rev.* 64 (2012), pp. 37–48; H. Mohwald. *Annu. Rev. Phys. Chem.* 41 (1990), pp. 441–476; S. Kewalramani *et al.* *J. Phys. Chem. Lett.* 1.2 (2010), pp. 489–495.

¹⁷ E. Pambou *et al.* *Langmuir* 31.36 (2015), pp. 9781–9789; D. W. Hayward *et al.* *Macromolecules* 48.5 (2015), pp. 1579–1591; I. Rodriguez-Loureiro *et al.* *Soft Matter* 13.34 (2017), pp. 5767–5777; G. Hazell *et al.* *J. Colloid Interface Sci.* 474 (2016), pp. 190–198.

¹⁸ O. Albrecht *et al.* *J. Phys. France* 39.3 (1978), pp. 301–313.

¹⁹ O. Kratky *et al.* *J. Colloid Sci.* 4.1 (1949), pp. 35–70.

²⁰ G. V. Jensen *et al.* *Angew. Chemie Int. Ed.* 53.43 (2014), pp. 11524–11528.

²¹ V. Rondelli *et al.* *J. Phys. Conf. Ser.* 340 (2012), p. 012083.

²² P. A. Hassan *et al.* *J. Colloid Interface Sci.* 257.1 (2003), pp. 154–162, see Section 2.2.7.

²³ R. A. Campbell *et al.* *J. Colloid Interface Sci.* 531 (2018), pp. 98–108; J. R. Lu *et al.* *Acta Crystallogr. A* 52.1 (1996), pp. 11–41, see Section 2.2.7.

²⁴ J. S. Pedersen. "Monte Carlo Simulation Techniques Applied in the Analysis of Small-Angle Scattering Data from Colloids and Polymer System". In: *Neutron, X-Rays and Light. Scattering*

²⁵ M. Wormington *et al.* *Philos. Trans. R. Soc. London Ser. A* 357.1761 (1999), pp. 2827–2848.

²⁶ Nelson *et al.*, “Refnx: Neutron and X-Ray Reflectometry Analysis in Python”, *op. cit.*

²⁷ Such as molecular dynamics.

²⁸ E. Scoppola *et al.* *Curr. Opin. Colloid Interface Sci.* 37 (2018), pp. 88–100.

²⁹ The historical context of this is discussed briefly in Chapter ??.

³⁰ S. Bowerman *et al.* *J. Chem. Theory Comput.* 13.6 (2017), pp. 2418–2429.

³¹ In the form of Empirical Potential Structure Refinement.

³² R. Hargreaves *et al.* *J. Am. Chem. Soc.* 133.41 (2011), pp. 16524–16536.

³³ M. T. Ivanović *et al.* *Angew. Chemie Int. Ed.* 57.20 (2018), pp. 5635–5639.

³⁴ A. F. Miller *et al.* *Mol. Phys.* 101.8 (2003), pp. 1131–1138; P. M. Anderson *et al.* *J. Chem. Phys.* 121.17 (2004), p. 8503.

³⁵ Monte Carlo and molecular dynamics respectively.

³⁶ A. P. Dabkowska *et al.* *Langmuir* 30.29 (2014), pp. 8803–8811.

³⁷ A. Koutsioubas. *J. Phys. Chem. B* 120.44 (2016), pp. 11474–11483.

timisation,²⁵ and Bayesian inference.²⁶ However, there has been little change in the definition of the models that unpin the analysis processes. Recently, there have been movements towards the use of atomistic modelling techniques²⁷ to augment, and assist, the analysis of soft matter scattering measurements, in a multi-modal approach.²⁸

Much of the work relating to the use of atomistic simulation for the analysis of small angle scattering measurements has been focused on the study of protein molecules in solution.²⁹ This has allowed for a more profound understanding aspects of biology such as the conformational states available to protein molecules in solution.³⁰ The uptake of atomistic simulation for the analysis of small angle scattering from systems such as micelles has been slower, in part due to the more complex conformation landscape available to these systems under standard conditions. However, the work of Hargreaves *et al.* paired atomistic simulation with total scattering measurements³¹ to resolve the structure of a simple short-tail surfactant micelle.³² Further, the work of Ivanović *et al.* used scattering experiments to refine the output of molecular dynamics simulations of micelles of a pre-defined size.³³ Both of these examples required significant computational resource; in the former case, the computational time taken was quoted as 200 days, while the later required the running of multiple simulations at different micelle sizes in order to determine the appropriate simulation.

The use of atomistic simulation for the analysis reflectometry measurements of soft matter systems began with the work of Miller *et al.* and Anderson and Wilson,³⁴ where atomistic simulations³⁵ were used to study polymer self-assembly at the oil-water interface. These simulation trajectories were then compared with experimental neutron reflectometry measurements. Dabkowska *et al.* also used atomistic simulation and neutron reflectometry measurements to study the structure of a surfactant monolayer at the air-water interface, providing the first example of a direct comparison between experimental reflectometry data and that determined from simulation.³⁶ To date, there is only one work that has used coarse-grained molecular dynamics simulation to aid in the analysis of neutron reflectometry, this is the work of Koutsioubas.³⁷ This work made use of the MARTINI coarse-grained forcefield to simulate a lipid bilayer, and was compared with experimental neutron reflectometry measurements.

1.3 COARSE-GRAINING OF SOFT MATTER SYSTEMS

The characteristic non-atomistic length scales associated with soft matter systems make them ideal for the application of coarse-graining protocols. Coarse-graining is where dimensionality of a problem is reduced by the removal of certain degrees of freedom

from a set. The most common method of coarse-graining is the re-parameterisation of an atomistic molecular dynamics potential model in terms of this reduced parameter space. An example of this is the MARTINI forcefield,³⁸ where the aim is to reparameterise the system without significant loss of chemical information.³⁹ A result of coarse-graining is the creation a flatter potential energy landscape, as shown in Figure 2.20. However, in this work I have also investigated the effect of applying a chemically-consistent coarse-grained monolayer model for the analysis of reflectometry data,⁴⁰ This system is coarse-grained so as to describe a phospholipid material as consisting of a head group and pair of tail groups. Additionally, I have assessed the efficacy of different atomistic and coarse-grained potential models for the analysis of neutron reflectometry, building on the work of Dabkowska *et al.* and Koutsioubas.⁴¹

1.4 OPTIMISATION METHODOLOGIES

The availability of high performance computing has increased significantly in recent years, in particular due to cloud-based infrastructures. Furthermore, highly parallelisable optimisation algorithms are now available such as the particle swarm⁴² and differential evolution⁴³ optimisations. As mentioned above, previous work has shown that the simulation of a surfactant micelle and comparison with experimental data requires significant computational expense⁴⁴ In the interest of reducing this, and improving the applicability of high performance computing to simulation-driven analysis of small angle scattering I have investigated the use of a particle swarm optimisation (PSO) to produce a realistic, near-atomistic micelle structure based on experimental data alone. This has made use of a coarse-grained description of a surfactant molecule on two levels; one for the particle swarm optimisation and another for the scattering profile calculation.⁴⁵

1.5 EDUCATIONAL MATERIALS

While the development of analytical methods and infrastructure are important for the development and uptake of the simulation-driven analysis methods applied in this work, the development of informatative resources is also necessary. Current experimental users of small angle scattering are typically not familiar with detailed aspects of classical simulation, however, they are often interested in applying it to assist with their analyses. Therefore, alongside traditional research applications, I have been developing open educational resources⁴⁶ designed to introduce classical simulation techniques, and to allow users of scattering techniques to become familiar with these. The ambition being that as the availability of simulation-driven analysis for small angle scattering

³⁸ This specific model is discussed in greater detail in Section 2.3.3.

³⁹ S. J. Marrink *et al.* *J. Phys. Chem. B* 111.27 (2007), pp. 7812–7824.

⁴⁰ This work is the focus of Chapter ??.

⁴¹ Dabkowska *et al.*, “Modulation of Dipalmitoylphosphatidylcholine Monolayers by Dimethyl Sulfoxide”, *op. cit.*; Koutsioubas, “Combined Coarse-Grained Molecular Dynamics and Neutron Reflectivity Characterization of Supported Lipid Membranes”, *op. cit.*, see Chapter ??.

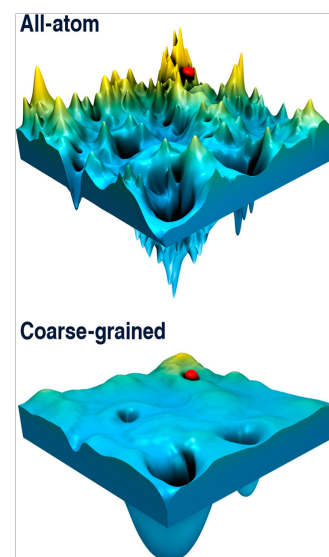


Figure 1.3: Potential energy surfaces for an all-atom vs a coarse-grained potential model, reprinted with permission of the American Chemical Society from S. Kmiecik *et al.* *Chem. Rev.* 116.14 (2016), pp. 7898–7936.

⁴² J. Kennedy *et al.* In: *Proceedings of ICNN'95. International Conference on Neural Networks*. Perth, AU, 1995, pp. 1942–1948; Y. Shi *et al.* In: *1998 IEEE International Conference on Evolutionary Computation Proceedings. IEEE World Congress on Computational Intelligence*. Anchorage, US, 1998, pp. 69–73.

⁴³ R. Storn *et al.* *J. Global Optim.* 11 (1997), pp. 341–359.

⁴⁴ Hargreaves *et al.*, “Atomistic Structure of a Micelle in Solution Determined by Wide Q -Range Neutron Diffraction”, *op. cit.*; Ivanović *et al.*, “Temperature-Dependent Atomic Models of Detergent Micelles Refined against Small-Angle X-Ray Scattering Data”, *op. cit.*

⁴⁵ See Chapter ??.

grows, so will the user base that is familiar with the underlying methods.⁴⁷

⁴⁷ See Chapter ??.

2

THEORY

2.1 PROBING RADIATION

This work is focussed on the use of X-ray and neutron scattering to probe soft matter systems; in particular surfactant monolayers and micelles. Therefore, it is pertinent to discuss how each of these probing radiation is produced and detail the advantages of each with respect to the other.

2.1.1 Generation of X-rays

X-rays are a form of electromagnetic radiation similar to visible light, albeit with a much shorter wavelength.¹ There are four common ways to produce X-rays; three are available within the laboratory, while the other is exclusive to large scale facilities.

The three laboratory source X-ray generation techniques are the X-ray tube, the rotating anode, and the liquid jet. An X-ray tube consists of a filament and an anode within a vacuum chamber, by passing a high voltage electrical current across the filament electrons are emitted which accelerate towards the anode. On collision with the anode, the rapid deceleration results in the emission of X-rays at a characteristic wavelength based on the anode material.² The most common material for an X-ray tube anode is copper which gives off radiation with an energy of ~ 8 keV.³

Another common laboratory method for the generation of X-rays is the rotating anode.⁴ In the X-ray tube, each time that an electron collides with anode there is some energy transfer, this means that over many millions of collisions the temperature of the anode can rise significantly, which can cause the anode material to melt. Resulting in a temperature-based limitation to the available X-ray flux. This lead to the development of the rotating anode, which is simply where the anode is made from a rotating wheel, such that the bombardment is spread across the whole wheel reducing the energy localisation. The use of a rotating anode can allow for an increase in the photon flux by about an order of magnitude.⁵

The final laboratory method for X-ray generation is the liquid jet source.⁶ For the liquid jet X-ray source, an electron beam is

¹ Typically 0.01-10 nm.

² H. Schnablegger *et al.* *The SAXS Guide: Getting Acquainted with the Principles*. 2017.

³ This is a wavelength of ~ 1.5 nm.

⁴ Essentially an improvement on the X-ray tube.

⁵ Schnablegger *et al.*, *The SAXS Guide: Getting Acquainted with the Principles*, op. cit.

⁶ *MetalJet X-Ray Source Technology*. URL: <https://www.excillum.com/technology/> (Accessed 2018-12-6), Branded MetalJet by excillum.

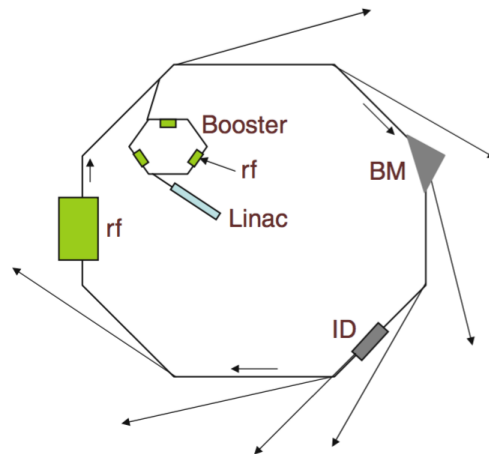
⁷ Usually an gallium or indium alloy.

⁸ Such as Diamond Light Source (DLS) or the European Synchrotron Radiation Facility (ESRF).

incident on a liquid metal sample,⁷ rather than traditional solid metal, which can dissipate heat more efficiently. This means that the electron intensity and therefore X-ray brightness, available to the liquid jet source is much greater than a rotating anode source.

The method of X-ray generation that is not available in a typical laboratory is at a synchrotron, the use of this method has the drawback that it requires access to a national or international facility.⁸ The way in which X-rays are generated at a synchrotron involves the acceleration of an electron, rather than the deceleration as with the laboratory sources. This is achieved by having relativistic electrons travel on a curve, from Newtonian mechanics it is known that travelling on a curve at constant speed is equivalent to acceleration. First the electrons are accelerated, after being produced in a linear accelerator, to near the speed of light in a booster synchrotron before injecting them into the storage ring. In the storage ring, the electrons are kept at relativistic speeds with bending magnets and straight sections making up a ring as shown in Figure 2.1. How circular the ring is depends on the number of bending magnets that make it up; for example, DLS had 48 bending magnets with 48 straight sections at the time of construction.

Figure 2.1: A schematic representation of a synchrotron radiation source, identifying the Linac, the booster ring, the radio-frequency cavities (rf), the bending magnet (BM) and the insertion device (ID). Reprinted, with permission of Springer Nature Customer Service Centre GmbH: Springer Nature, from M. C. Garcia-Gutierrez *et al.* "Bases of Synchrotron Radiation, Light Sources, and Features of X-Ray Scattering Beamlines". In: *Applications of Synchrotron Light to Scattering and Diffraction in Materials and Life Sciences*. 2009, pp. 1–22.



When an electron accelerates (or travels on a curve), Cherenkov radiation is emitted in accordance with the Cherenkov relation,

$$n_i \beta_c \cos \theta_e = 1, \quad (2.1)$$

where, n_i is the refractive index for the dielectric medium, β_c is the fraction of the speed of light at which that electron is travelling, and θ_e is the angle between the electron trajectory and the trajectory of the resulting photon.⁹ The curve is the result of a bending magnet, meaning that at each bending magnet there can be a beamline which uses the synchrotron light. The light that is given off from a bending magnet is continuous and broad, covering a wide range of the electromagnetic spectrum. The alternative to a bending magnet beamline is that which is served by an insertion device.

⁹ M. C. Garcia-Gutierrez *et al.* "Bases of Synchrotron Radiation, Light Sources, and Features of X-Ray Scattering Beamlines". In: *Applications of Synchrotron Light to Scattering and Diffraction in Materials and Life Sciences*. 2009, pp. 1–22.

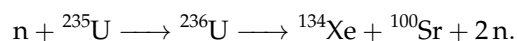
An insertion device is able to offer more specific radiation characteristics (photon energy, narrower band) than a bending magnet, and are placed on the straight sections of the synchrotron. Common insertion devices include wavelength shifters, wigglers, and undulators.

The type of insertion device that is present at both I07 and I22 at DLS is an undulator. An undulator consists of a series of magnets of opposing polarity that causes the electrons to ‘wiggle’ back and forth as shown in Figure 2.2. This results in a superposition of radiation from N_P sources, where N_P is the number of magnets, yielding quasi-monochromatic radiation. The brilliance of different X-ray sources are compared in Table 2.1, this shows the significant benefit that an undulator can offer in terms of photon brilliance.

2.1.2 Generation of neutrons

Neutrons hold an advantage over X-rays, particularly for application to the study of soft matter, due to the ability to use contrast variation to increase the quantity of information from the sample.¹⁰ However, neutrons cannot be produced safely on a laboratory scale, therefore it is always necessary to visit large scale facilities to harness neutrons for scattering experiments. These facilities come in two flavours; the reactor source and the spallation source, each offering unique benefits.

Neutron reactor sources¹¹ are currently the most common format of neutron source and are capable of producing the highest average neutron flux.¹² The High-Flux Reactor at the ILL is capable of producing a neutron flux of 1.5×10^{15} neutrons $\text{s}^{-1}\text{cm}^{-2}$.¹³ A reactor source operates on the principle of nuclear fission, where an atomic nucleus is capable of breaking down into smaller nuclei, overcoming the strong nuclear force. This often involves using uranium enriched with its fissile isotope, ^{235}U , which after the initial absorption of a stray neutron¹⁴ will undergo fission to release, on average, 2.5 daughter neutrons, an example of a possible uranium fission mechanism is:



This type of mechanism is the basis for both research, and nuclear power, reactors.¹⁵ One of the major drawbacks for reactor neutron sources is the perceived public opinion towards such facilities. Major safety concerns, such as “nuclear meltdown” and the resulting

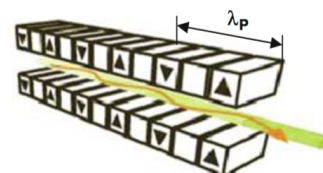


Figure 2.2: A diagram of an undulator insertion device, such as that on I07 and I22, where λ_P is the period length between opposing magnets. Reprinted, with permission of Springer Nature Customer Service Centre GmbH: Springer Nature, from Garcia-Gutierrez *et al.*, “Bases of Synchrotron Radiation, Light Sources, and Features of X-Ray Scattering Beamlines”, op. cit.

¹⁰ This is discussed in detail in Section 2.2.8.

¹¹ Such as the Institut Laue-Langevin (ILL) in Grenoble, France.

¹² The number of neutrons per second per unit area.

¹³ ILL: Neutron for Science: Technical Characteristics. URL: <https://www.ill.eu/reactor-environment-safety/high-flux-reactor/technical-characteristics/> (Accessed 2016-8-8).

¹⁴ Arising from a cosmic ray, or spontaneous fission.

¹⁵ D. S. Sivia. *Elementary Scattering Theory: For X-Ray and Neutron Users*. 2011.

Light source	Approximate brilliance/ photons $\text{s}^{-1}\text{mrad}^{-2}0.1\%\text{bandwidth}^{-1}$
Candle	1×10^5
X-ray tube	1×10^8
Sun	1×10^{10}
Bending magnet	1×10^{15}
Undulator	1×10^{20}

Table 2.1: A comparison of the photon brilliance from different light sources. Adapted, with permission of Oxford University Press, from D. S. Sivia. *Elementary Scattering Theory: For X-Ray and Neutron Users*. 2011.

nuclear waste, mean that reactor sources are often unpopular and therefore struggle to obtain funding required for operation.

The other form of neutron source is a spallation source, this is much less controversial as it does not require fissile materials and hence there is no risk of a nuclear disaster. The ISIS Neutron and Muon Source is an example of a spallation source, where high energy protons, 800 MeV,¹⁶ are accelerated towards a tungsten target. When the protons strike the target, they can cause the release of a series of neutrons, the first batch of neutrons are given off with too high an energy to be useful, however, less excited neutrons are given off by secondary emissions. In addition to the public perception benefit, spallation sources also offer a technological advantage in the time-of-flight¹⁷ technique. The ToF technique relies the fact that at a spallation source, it is possible to know the time at which the neutron was ejected from the target to a high level of precision and therefore it is possible to measure the time taken for the neutron to reach the instrument. Since the neutron is a particle of a finite mass, m , it is possible to correlate the velocity, \mathbf{v} , of the particle with the kinetic energy, E_k ,

$$E_k = \frac{m\mathbf{v}^2}{2}, \quad (2.2)$$

and with knowledge of the energy of the particle, its wavelength, λ , can be determined by the de Broglie relation,¹⁸

$$E = h\omega = \frac{h\mathbf{v}}{\lambda}, \quad (2.3)$$

where, h is Planck constant and ω is the neutron frequency. Therefore, the wavelength of the neutron is proportional to the inverse of the particle's velocity, and hence the time-of-flight, t_F ,

$$\lambda = \frac{h}{m\mathbf{v}} = \frac{ht_F}{mL_F}, \quad (2.4)$$

where, L_F is the distance between the target and the instrument. The fact that the neutrons can spread out in the flight from the target means that wavelength-dispersive techniques, where the neutron wavelength is measured rather than the scattering angle, are possible at spallation sources which cannot be carried out natively at reactor sources. The weakness of current spallation sources is that they have a lower average flux than reactor sources, however, the construction of the European Spallation Source¹⁹ will change this as it offers an average flux similar to that of a reactor source with the benefits of the spallation technique.

A problem that is inherent for both reactor and spallation sources is that the energy of the neutrons given off is usually too high to be used to study condensed materials, such as soft matter. This means that moderation must be used to reduce the energy of the neutrons passing through the sample. The neutrons that are considered to be optimal for the study of condensed materials are

¹⁶ *ISIS – How ISIS Works*. URL: <https://www.isis.stfc.ac.uk/Pages/What-does-ISIS-Neutron-Muon-Source-do.aspx> (Accessed 2018-9-25).

¹⁷ Abbreviated to ToF.

¹⁸ L. de Broglie. *Ann. Phys. (Paris)* 10.3 (1925), pp. 22–125.

¹⁹ Known as the ESS.

thermal in nature, named because their energy is approximately that of ambient temperature. Thermal neutrons are achieved by allowing the neutrons to pass through a large volume of moderator material, usually, graphite, D_2O , methane or H_2 , stored at 300 K before they reach the instrument.²⁰

²⁰ Sivia, *Elementary Scattering Theory: For X-Ray and Neutron Users*, op. cit.

2.2 SCATTERING

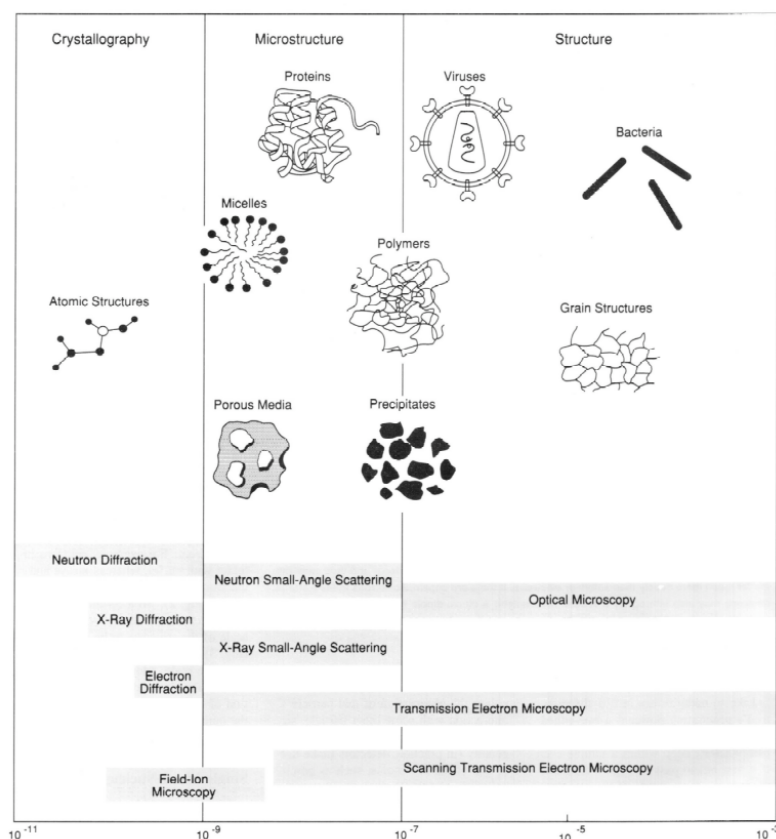


Figure 2.3: A representation of how different techniques can be used to probe various length scales. Reprinted, with permission of Oxford University Press, from D. S. Sivia. *Elementary Scattering Theory: For X-Ray and Neutron Users*. 2011.

The use of scattering techniques to probe soft condensed matter systems is commonplace. In this work, we have focussed on the use of small angle scattering²¹ and reflectometry techniques. These are particularly appropriate for application to soft condensed matter systems due to the length scales capable of being probed being similar to the persistence length of the soft condensed matter systems. The length scale covered for such techniques is from around 1-300 nm, as is shown in Figure 2.3. The focus is on the equilibrium structure(s) of a material, and therefore there is no interest in the system dynamics, meaning that exclusively elastic scattering techniques may be used, where there is no energy transfer between the probing radiation and the material. This is in contrast to inelastic scattering where energy transfer occurs; facilitating the measurement of system dynamics, such as the dynamical modes of

²¹ Generally abbreviated to SAS; with SAXS indicating the use of X-rays and SANS neutrons

²² V. Garcia Sakai *et al.* *Curr. Opin. Colloid Interface Sci.* 14.6 (2009), pp. 381–390; B. Farago. *Curr. Opin. Colloid Interface Sci.* 14.6 (2009), pp. 391–395.

²³ See Section 2.2.8.

²⁴ Not just X-rays and neutrons, but any wave.

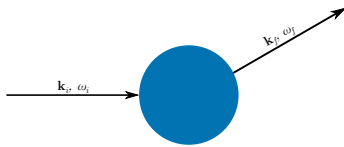


Figure 2.4: A schematic of the scattering of some probing radiation by a sample (blue circle). Adapted, with permission of Oxford University Press, from Sivia, *Elementary Scattering Theory: For X-Ray and Neutron Users*, op. cit.

²⁵ Throughout this work, units of \AA^{-1} will be wherever possible.

polymers and lipid bilayers²²

Both X-ray and neutron scattering techniques are discussed and used in this work. From an experimental viewpoint, there are significant differences between an X-ray scattering and a neutron scattering experiment. However, there is little variation in terms of the data analysis, where the differences are limited to; the nature of the scattering lengths²³ and the higher background that is present in the neutron scattering experiments.

2.2.1 The scattering vector

The scattering of some probing radiation,²⁴ by some sample, can be represented as shown in Figure 2.4. Since only elastic scattering is being considered, there will be no change in the frequency of the radiation, $\omega_i = \omega_f$. This means that only the wavevector, \mathbf{k} , can change, $\mathbf{k}_i \neq \mathbf{k}_f$. The difference between the incident and final wavevectors is the scattering vector, \mathbf{q} , where,

$$\mathbf{q} = \mathbf{k}_i - \mathbf{k}_f. \quad (2.5)$$

The scattering vector strictly has units of m^{-1} , however it is often more practical to use nm^{-1} or \AA^{-1} .²⁵ Since the frequency of the probing radiation does not change during an elastic scattering event, the wavelength, λ , will also not change, meaning that the moduli of the incident and final wavevectors are,

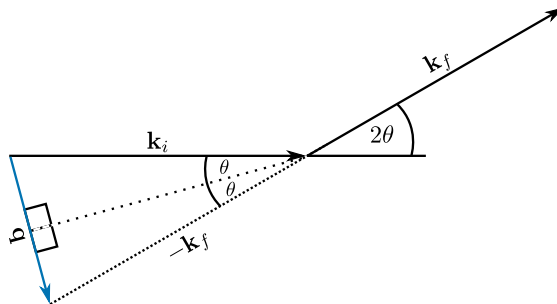
$$|\mathbf{k}_i| = |\mathbf{k}_f| = \frac{2\pi}{\lambda}. \quad (2.6)$$

This also means that only the angle will change during the elastic scattering event. The vector diagram in Figure 2.5 can be used to describe the geometry of an elastic scattering event. From this, and Equation 2.6, the value of q , where $q = |\mathbf{q}|$ can be shown as,

$$q = \frac{4\pi \sin \theta}{\lambda}. \quad (2.7)$$

However, this fails to fully capture the three dimensional nature

Figure 2.5: A vector diagram describing an elastic scattering event, where \mathbf{k}_i is the incident wavevector, \mathbf{k}_f is the final wavevector, 2θ is the scattering angle, and \mathbf{q} is the scattering vector. Adapted, with permission of Oxford University Press, from D. S. Sivia. *Elementary Scattering Theory: For X-Ray and Neutron Users*. 2011.



of the scattering event. Hence, it is necessary to describe the scattering with spherical coordinates, 2θ , and ϕ , such that the incoming

and outgoing radiation can be described as,

$$\begin{aligned}\mathbf{k}_i &= \left(0, 0, \frac{2\pi}{\lambda}\right), \\ \mathbf{k}_f &= \frac{2\pi}{\lambda}(\sin 2\theta \cos \phi, \sin 2\theta \sin \phi, \cos 2\theta),\end{aligned}\quad (2.8)$$

where, $|\mathbf{k}_f| = 2\pi/\lambda$. This allows the scattering vector to be written,

$$\mathbf{q} = \frac{4\pi \sin \theta}{\lambda}(-\cos \theta \cos \phi, -\cos \theta \sin \phi, \sin \theta). \quad (2.9)$$

For an isotropic scattering pattern, it is the magnitude of the scattering vector, q , that is measured. In practical terms, the scattering vector allows for easy comparison of measurements made at different radiation wavelengths.

The basic quantity measured in a scattering experiment is the differential cross section, $d\sigma(q)/d\Omega$. This is the fraction of particles of probing radiation that is scattered with a particular set of polar coordinates, 2θ and ϕ ,

$$\frac{d\sigma(q)}{d\Omega} = \frac{R_i(2\theta, \phi)}{NV\Phi\Delta\Omega}, \quad (2.10)$$

where, $R_i(2\theta, \phi)$ is the rate of arrival of the scattered particles at the position $2\theta, \phi$, V is the illuminated volume of the sample, Φ is incident flux, $\Delta\Omega$ is some small solid angle, and N is the number of scattering particles of interest, in the case of elastically scattered radiation, $N = N\%_{\text{el}}$, where $\%_{\text{el}}$ is the fraction of elastically scattered radiation.

2.2.2 Scattering from a single fixed particle

It is possible to describe a steady stream X-ray photons or neutrons of wavelength, λ , travelling through space as follows,

$$\psi_i = \psi_o \exp(\mathbf{i}kz), \quad (2.11)$$

where, z is the direction of travel, and the incident flux is the magnitude of the wave squared, $\Phi = |\psi_o|^2$. This wave then interacts with a single fixed particle elastically, propagating the wave radially outwards, as shown in Figure 2.6. This propagation is centred on the atom, therefore the wavevector, \mathbf{k}_f is parallel to the displacement vector, \mathbf{r} , and the following holds,

$$\exp(\mathbf{i}\mathbf{k}_f \cdot \mathbf{r}) = \exp(\mathbf{i}kr). \quad (2.12)$$

This final wave is no longer collimated and therefore diminishes with distance, r . Hence the final scattered wave has the form,

$$\psi_f = \psi_o b \frac{\exp(\mathbf{i}kr)}{r}, \quad (2.13)$$

where, b is the scattering length discussed in Section 2.2.8.

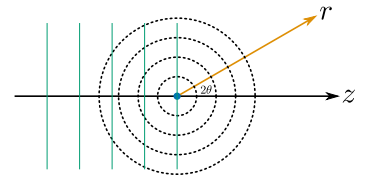


Figure 2.6: A schematic showing the propagation of the wave of probing radiation (green lines) radially outwards following the scattering event, where r is the magnitude of the displacement vector. Adapted, with permission of Oxford University Press, from *ibid*.

2.2.3 Scattering from multiple particles

It is important to consider how the probing radiation would interact with a real system, consisting of many particles. If the incident beam has the form of Equation 2.11, with the wavevector $\mathbf{k}_i = (0, 0, k)$, each particle, j , will contribute the following to the total scattered wave, ψ_f , made up of the scattering from all, N , atoms,

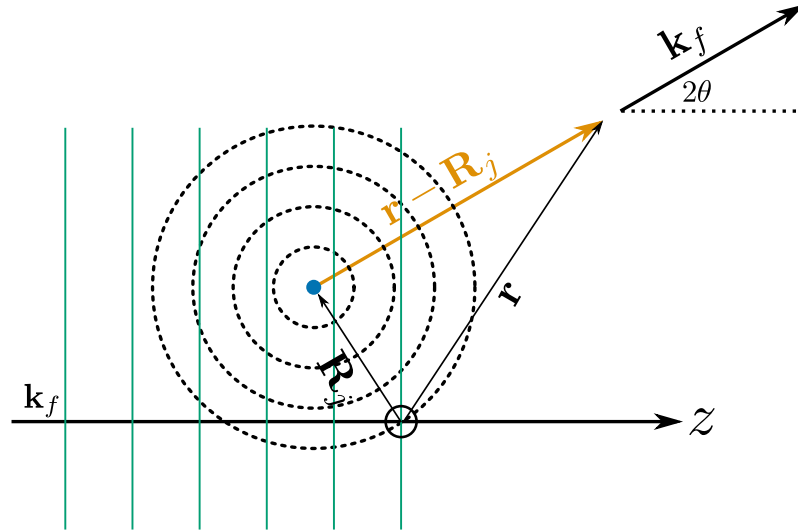
$$[\delta\psi_f]_j = \psi_o \exp(\mathbf{i}\mathbf{k}_i \cdot \mathbf{R}_j) b_j \frac{\exp\{\mathbf{i}\mathbf{k}_f \cdot (\mathbf{r} - \mathbf{R}_j)\}}{|\mathbf{r} - \mathbf{R}_j|}, \quad (2.14)$$

where, \mathbf{R}_j is the position of particle j , \mathbf{r} is some arbitrary position, and \mathbf{k}_f is the wavevector of the scattered wave, described graphically in Figure 2.7. This allows the total scattered wave to be defined as a summation of the contributions from the individual waves,

$$\psi_f = \psi_o \exp(\mathbf{i}\mathbf{k}_f \cdot \mathbf{r}) \sum_{j=1}^N \left\{ b_j \frac{\exp(\mathbf{i}\mathbf{q} \cdot \mathbf{R}_j)}{|\mathbf{r} - \mathbf{R}_j|} \right\}. \quad (2.15)$$

Equation 2.15 holds true, within the Born approximation, where the scattered wave has no impact on the incident wave and each wave is scattered only once.

Figure 2.7: A schematic showing the interaction of radiation scattered by two particles that are separated by the vector \mathbf{R}_j . Adapted, with permission of Oxford University Press, from D. S. Sivia. *Elementary Scattering Theory: For X-Ray and Neutron Users*. 2011.



The sample-detector distance is usually much larger than the typical particle size, allowing for the following approximation,

$$|\mathbf{r} - \mathbf{R}_j| = |\mathbf{r}| = r. \quad (2.16)$$

This is termed the Fraunhofer, or far-field limit, and allows Equation 2.15 to be simplified,

$$|\psi_f|^2 = \frac{\Phi}{r^2} \left| \sum_{j=1}^N b_j \exp(\mathbf{i}\mathbf{q} \cdot \mathbf{R}_j) \right|^2. \quad (2.17)$$

In the scattering experiment, radiation is deflected elastically into a detector with a small area, δA , at the polar coordinates, 2θ and ϕ , at a rate of R_{el} ,

$$R_{\text{el}}(2\theta, \phi) = |\psi_f|^2 \delta A = \Phi \delta \Omega \left| \sum_{j=1}^N b_j \exp(\mathbf{i}\mathbf{q} \cdot \mathbf{R}_j) \right|^2, \quad (2.18)$$

where, $\delta \Omega = \delta A / r^2$. Therefore, the differential cross section, defined in Equation 2.10 can be related to the scattering from the sample as,

$$\left(\frac{d\sigma(q)}{d\Omega} \right)_{\text{el}} = \frac{1}{V} \left| \sum_{j=1}^N b_j \exp(\mathbf{i}\mathbf{q} \cdot \mathbf{R}_j) \right|^2. \quad (2.19)$$

2.2.4 Scattering length density

While it may be helpful to consider the scattering from multiple particles individually, where each particle has a scattering length, b . In practice, due to low experimental resolution at small angles, it is more common to consider the scattering length density,²⁶ of the system,

²⁶ Abbreviated to SLD.

$$\text{SLD} = \frac{1}{V} \sum_{i=0}^N b_i, \quad (2.20)$$

where N is the total number of particles in the volume V . A result of this equation is the ability to rewrite Equation 2.19 as,

$$\left(\frac{d\sigma(q)}{d\Omega} \right)_{\text{el}} = \frac{1}{V} \left| \iiint_V \text{SLD} \exp(\mathbf{i}\mathbf{q} \cdot \mathbf{R}) d^3\mathbf{R} \right|^2. \quad (2.21)$$

This equation shows that the scattering differential cross-section from some object is related to the scattering length density profile of that object by a Fourier transform.

2.2.5 Model-dependent analysis

All types of scattering patterns can be analysed by two methods; model independent and model-dependent. The nature of this work means that it will focus on model-dependent analysis methods.²⁷ Model-dependent analysis has significant benefits over model-independent methods, such as improved resolution and more detailed information about the structure. However, the necessity of the inclusion of *a priori* information within model-dependent analysis may act to bias the result. While this is undesirable, these assumptions can, and should, be educated based on the chemical information present.²⁸

²⁷ With the model usually being derived from some atomistic, or coarse-grained simulation.

The scattering from the model system is determined, using technique specific methods that are discussed in detail in later sections. This is then compared with the experimental data using some figure of merit, the model is then varied to find the best possible model for the data provided.²⁹ In order to accurately reproduce

²⁸ A. R. McCluskey *et al.* *Curr. Org. Chem.* 22.8 (2018), pp. 750–757, such as the propensity for twin-tailed lipid molecules to form monolayers at an air-water interface or small surfactants to form micelles in solution.

²⁹ This typically uses some optimisation algorithm to determine the best solution, the particular algorithms used in this work are discussed in Section 2.4.

the experimental measurement, it is necessary to include some instrumental resolution function, $res(q)$, in the modelling procedure. This is instrument-specific, although it may be approximated by convolving the experimental dataset with some Gaussian smearing function, the modelled intensity can then be determined from,³⁰

$$I(q) = res(q) * \frac{d\sigma(q)}{d\Omega}, \quad (2.22)$$

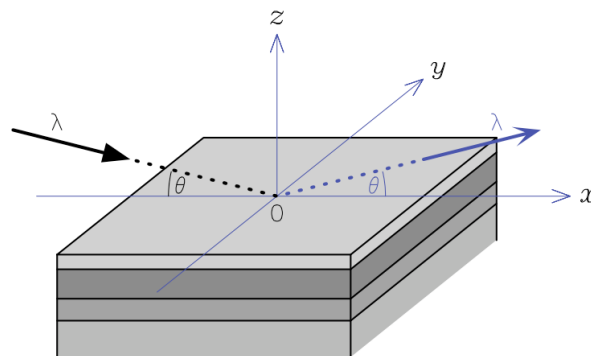
where, $d\sigma(q)/d\Omega$ is the differential cross-section, a measure of the number of scattering particles hitting a given solid angle of the detector.

The aim of model-dependent analysis is to obtain a model for the system which agrees well with the experimentally measured scattering data while producing something that is chemically and physically relevant.

2.2.6 Reflectometry

Reflectometry involves the interaction of the probing radiation with some interface, from which the radiation is reflected. The geometry of a reflectometry experiment is shown in Figure 2.8, where the reflectometry instrument is in the horizontal configuration, ideal for the study of liquid interfaces.³¹ Reflectometry measurements give information about the structure perpendicular to the interface, the z -dimension in Figure 2.8, and therefore the analysis of reflectometry data is founded on the assumption that the layers will be completely homogenous in the plane of the interface, the xy -plane in Figure 2.8. In reality, since the layers are usually not completely homogeneous, an average is obtained for the area in the radiation beam.

Figure 2.8: A schematic showing the geometry of a typical specular reflectometry experiment from a layered sample. Reprinted, with permission of Oxford University Press, from D. S. Sivia. *Elementary Scattering Theory: For X-Ray and Neutron Users*. 2011.



A reflectometry instrument operates by measuring the intensity of specular radiation at a series of different angles, θ , or wavelengths, λ . The reflected intensity is described in terms of the q -vector³², and is defined as follows,

$$R(q) = \frac{\text{specular reflected radiation intensity at } q}{\text{incident radiation intensity}}. \quad (2.23)$$

³⁰ A. R. J. Nelson *et al.* *J. Appl. Crystallogr.* 46.5 (2013), pp. 1338–1346; A. R. J. Nelson. *J. Appl. Crystallogr.* 47.3 (2014), p. 1162.

³¹ Such as those investigated in Chapters ?? and ??.

³² Using Equation 2.7

It is clear from Equation 2.23 that the value of the measured reflectometry cannot be greater than one, as this would mean that more particles of probing radiation were being reflected than were incident.

There are two model-dependent analysis techniques that can be applied to the understanding of a reflectometry dataset. The first is the kinematic approach, which can be described with Equation 2.19, from the assumption that $q_x = 0$ and $q_y = 0$, as we are only measuring the specular scattering. This approach models the reflectometry as a function of the scattering length density profile in the z -dimension, $SLD(z)$,

$$R(q) \approx \frac{16\pi^2}{q^4} \left| \int_{-\infty}^{+\infty} \frac{dSLD(z)}{dz} \exp(-izq_z) dz \right|^2, \quad (2.24)$$

where, $dSLD(z)/dz$ is the first derivative of the scattering length density profile. However, this method has a significant problem, which can be demonstrated by applying Equation ?? to the scattering length density profile of a bare silicon substrate, which can be modelled as a Heaviside function, as shown in Figure 2.9(a),

$$SLD(z) = \begin{cases} 0, & \text{where } z < 0 \\ SLD_{Si}, & \text{otherwise} \end{cases} \quad (2.25)$$

where, SLD_{Si} is the scattering length density of pure silicon.³³ The derivative of a stepwise Heaviside function is a scaled δ -function, as shown in Figure 2.9(b),

$$SLD'(z) = SLD_{Si} \delta(z). \quad (2.26)$$

Then, as in Equation ??, the Fourier transform of this δ -function is taken,

$$SLD_{Si} \int_{-\infty}^{+\infty} \delta(z) \exp(-izq_z) dz = SLD_{Si} \exp(0) = SLD_{Si}. \quad (2.27)$$

This means that, using Equations 2.27 and ??, the reflectometry profile could be calculated from the following relationship,

$$R(q) \approx \frac{16\pi^2 SLD_{Si}^2}{q_z^4}. \quad (2.28)$$

The curve from this relationship is shown in Figure 2.9, where it is clear that the agreement with an experimental profile would be poor as $q \rightarrow 0$. It can be seen that for low values of q the calculated reflectometry is greater than 1, which violates the physical constraint imposed with Equation 2.23. This break down of the kinematic approach is due to the assumption present in this approach that the Born approximation³⁴ will hold. However, in the reflectometry scattering geometry, this is no longer true rendering the kinematic approach invalid.

This breakdown of the kinematic approach has led to the application of the Abeles, or Parratt, model for the reflection of light

³³ This is $2.1 \times 10^{-6} \text{ \AA}^{-2}$ for neutrons.

³⁴ Mentioned previously in Section 2.2.3.

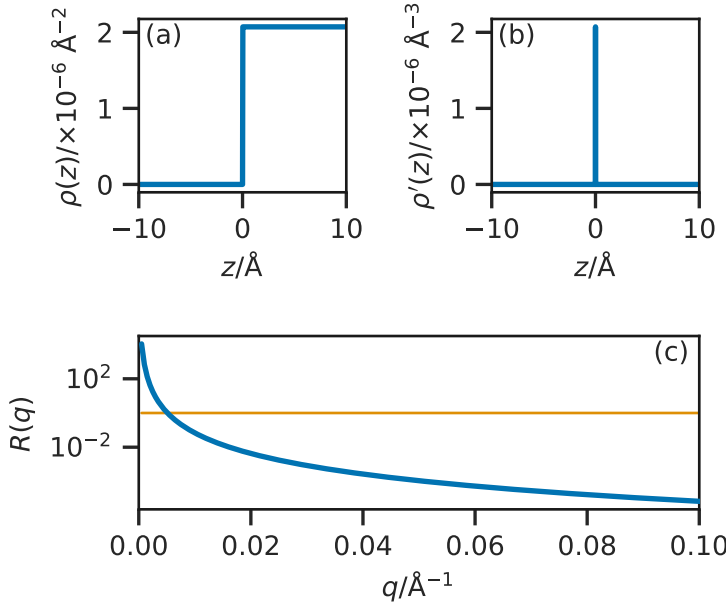


Figure 2.9: A graphical representation of the kinematic approach; (a) the Heaviside function describing the scattering length density profile of a bare silicon substrate, (b) the δ -function arising from the first derivative of the function in (a), and (c) the reflectometry profile resulting from the kinematic approach, where the orange line at $R = 1$ identifies the break down between experimental and theory in the kinematic approach. Adapted, with permission of Oxford University Press, from D. S. Sivia. *Elementary Scattering Theory: For X-Ray and Neutron Users*. 2011.

³⁵ F. Abelès. *Ann. Phys.* 12.3 (1948), pp. 504–520; L. G. Parratt. *Phys. Rev.* 95.2 (1954), pp. 359–369, also known as dynamical theory.

³⁶ Such as that between layers 0 and 1 in Figure 2.10.

at a given number of stratified interfaces.³⁵ This method involves considering the system as a layered structure at the interfaces of which, the probing radiation can either be reflected or refracted, by some refractive index, n_i . Figure 2.10 shows this process for a system of two layers, where the layer 0 is the air or vacuum above the sample, it is clear to see how the two waves labelled r could interfere constructively or destructively depending on the thickness of layer 1, d . This means that for a single interface,³⁶ the reflectometry can be described by the Fresnel equation,

$$R(q) = \left| \frac{n_0 \sin \theta_0 - n_1 \sin \theta_1}{n_0 \sin \theta_0 + n_1 \sin \theta_1} \right|^2. \quad (2.29)$$

Additionally at the point of total reflection, where $\theta_0 = \theta_c$, the critical angle, there will be no transmitted wave so,

$$n_1 \sin \theta_1 = 0, \quad (2.30)$$

and therefore the reflected radiation will never be greater than 1, while the critical angle can be defined as,

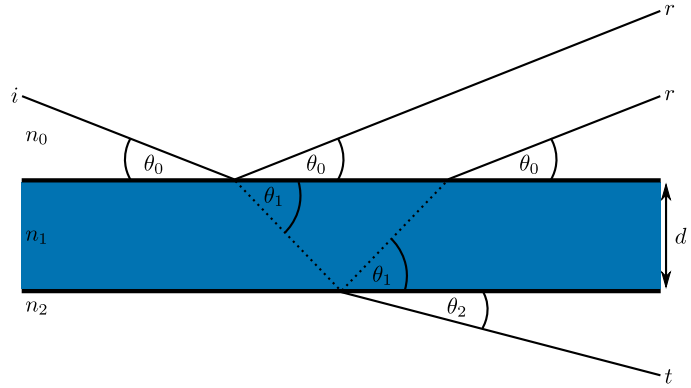
$$\cos^2 \theta_c = \frac{n_1^2}{n_0^2}. \quad (2.31)$$

This is the angle below which a reflectometry profile will be measured.

The above method can then be generalised to a structure of an arbitrary number of layers, as shown in Code Block 2.1.³⁷ For each value of q for which the reflectometry is to be calculated, the system is considered in terms of n_{\max} layers. The incident radiation

³⁷ The purpose of the Code Blocks throughout this work is to ensure transparency and reproducibility, these are written as Python functions with a standard docstring at the start describing the function and inputs.

Figure 2.10: A schematic diagram showing the reflected (r) and transmitted (t) waves when an incident (i) wave enters an interface of thickness d , where the refractive indices of each layer are n_0 , n_1 , and n_2 . Adapted, with permission of Elsevier, from F. Foglia *et al. Curr. Opin. Colloid Interface Sci.* 20.4 (2015), pp. 235–243.



beam will be refracted by each of the layers, giving wavevector values for each layer, k_n ,

$$k_n = \sqrt{k_0^2 + 4\pi(\text{SLD}_n - \text{SLD}_0)}, \quad (2.32)$$

where, $k_0 = q/2$. The Fresnel equation coefficient between layers n and $n + 1$, $r_{n,n+1}$ can then be found along with the phase factor, β_n , which is dependent on the thickness of the layer, d_n ,

$$r_{n,n+1} = \frac{k_n - k_{n+1}}{k_n + k_{n+1}}, \quad (2.33)$$

$$\beta_n = k_n d_n. \quad (2.34)$$

This means that a matrix can be evaluated for each layer, M_n ,

$$M_n = \begin{bmatrix} \exp \beta_n & r_{n,n+1} \exp -\beta_n \\ r_{n,n+1} \exp \beta_n & \exp -\beta_n \end{bmatrix} \quad (2.35)$$

The resultant matrix, B , is then found as a product of the matrix from each layer,

$$B = \prod_{n=0}^{n_{\max}} M_n, \quad (2.36)$$

and from this the reflected intensity at the given value of q can be found,

$$R(q_z) = \frac{B_{1,2}}{B_{1,1}}. \quad (2.37)$$

This algorithm models the layers as perfectly flat layers, which will not be strictly true.³⁸ This resulted in the correction term being added to Equation 2.33 to account for the roughness of the layers. This adapts Equation 2.33 to the form,

$$r_{n,n+1} = \frac{k_n - k_{n+1}}{k_n + k_{n+1}} \exp(-2k_n k_{n+1} \sigma_{n,n+1}^2), \quad (2.38)$$

where, $\sigma_{n,n+1}$ is the interfacial roughness between layers n and $n + 1$.³⁹ This has the effect of Gaussian broadening the layers into each other, as a result. This method⁴⁰ is currently implemented in a variety of reflectometry modelling software packages, such as

³⁸ Particularly for soft matter systems.

³⁹ L. Nénot *et al. Rev. Phys. Appl. (Paris)* 15.3 (1980), pp. 761–779.

⁴⁰ That is given programmatically in Code Block 2.1.

⁴¹ Nelson *et al.*, “Refnx: Neutron and X-Ray Reflectometry Analysis in Python”, op. cit.; A. R. J. Nelson. *J. Appl. Crystallogr.* 39.2 (2006), pp. 273–276; A. V. Hughes. *RasCAL*. URL: <https://sourceforge.net/projects/rscl/> (Accessed 2016-8-8); Y. Gerelli. *J. Appl. Crystallogr.* 49.1 (2016), pp. 330–339; Y. Gerelli. *J. Appl. Crystallogr.* 49.2 (2016), pp. 712–712.

Code Block 2.1: An example Python code block for the Abelès method for the calculation of reflectometry, adapted from A. R. J. Nelson *et al. J. Appl. Crystallogr.* 52.1 (2019), pp. 193–200.

refnx, MOTOFIT, RasCAL, and Aurore.⁴¹ Applying this method to the scattering length density profile shown in Figure 2.9 gives the reflectometry profile shown with the dashed green line in Figure 2.11.

```
# Copyright 2015–2019 A. R. J. Nelson
# Australian Nuclear Science and Technology Organisation
# Licensed under the BSD 3-Clause "New" or "Revised" License

import numpy as np

def abeles(q_values, sld, d):
    """
    Calculates the reflectometry from a set of layers of a given
    scattering length density.

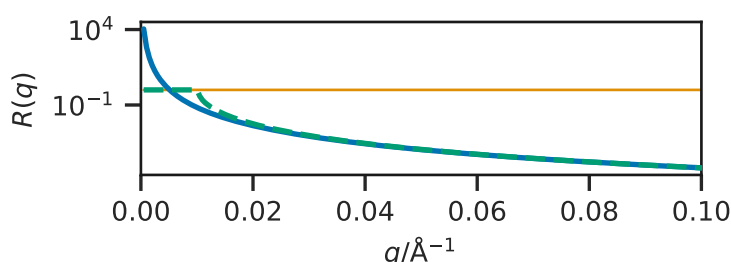
    Parameters
    -----
    q_values: float, array-like
        The q-vector values over which the reflectometry is to be
        calculated.
    sld: float, array-like
        An array of scattering length densities of length N, where
        N is the number of layers present.
    d: float, array-like
        An array of thicknesses of length N, where N is the number
        of layers present.

    Returns
    -----
    float, array-like
        The reflected intensity over the given q-vector values.
    """
    R = np.zeros_like(q_values)
    kn = np.sqrt(
        q_values[:, np.newaxis] ** 2.0 / 4.0 - 4.0 * np.pi * sld
    )
    B = np.zeros((2, 2, q_values.size))
    B[0, 0, :] = 1
    B[1, 1, :] = 1
    k = kn[:, 0]
    nmax = sld.size
    for n in range(1, nmax):
        kn1 = kn[:, n]
        r = (k - kn1) / (k + kn1)
        betan = k * d[n]
        if n > 0:
            Mn = np.array(
                [
                    [np.exp(betan * 1j), r * np.exp(betan * 1j)],
                    [r * np.exp(-betan * 1j), np.exp(-betan * 1j)]
                ]
            )
        else:
            Mn = np.array([[1, r], [r, 1]])
        p0 = B[0, 0, :] * Mn[0, 0, :] + B[1, 0, :] * Mn[0, 1, :]
        p1 = B[0, 0, :] * Mn[1, 0, :] + B[1, 0, :] * Mn[1, 1, :]
        B[0, 0, :] = p0
        B[1, 0, :] = p1
        p0 = B[0, 1, :] * Mn[0, 0, :] + B[1, 1, :] * Mn[0, 1, :]
        p1 = B[0, 1, :] * Mn[1, 0, :] + B[1, 1, :] * Mn[1, 1, :]
        B[0, 1, :] = p0
        B[1, 1, :] = p1
        k = kn1
    R = (B[0, 1, :] * np.conj(B[0, 1, :])) / (
        B[0, 0, :] * np.conj(B[0, 0, :])
    )
    R[np.where(np.isnan(R))] = 1.0
    return np.real(R)
```

2.2.7 Small angle scattering

Equation 2.21 identified that the scattering differential cross-section for some object was related to the SLD by a Fourier transform, which is shown graphically in Figure 2.12. This figure shows that there is a reciprocal relationship between the size of the object and the scattered intensity, decaying significantly up to values of $2\pi/d_x$, where d_x is the size of the object. This means that in order to probe large-scale structural features that are of interest in the study of soft materials, it is necessary to consider small values of q . When considering the nature of q in Equation 2.7, it is clear that such experiments would benefit from small values of θ and large values of λ . Hence, the use of scattering at small angles.

Figure 2.11: A comparison of the kinematic approach (blue solid line), and the dynamical approach (green dashed line), to determine the reflected intensity from the material with the scattering length density profile given in Figure 2.9(a). It is clear that at low q , there is a noticeable deviation between the two.



A SAS experiment generally involves some sample being placed in the path of the probing radiation; the scattering pattern that results from this transmission is measured at some distance, as is shown in Figure 2.13 for the D22 SANS instrument of the ILL. SAS instruments are usually very large, due to the large post sample flight path that is necessary to reach the small angles being measured.⁴² Transmission SAS can provide information about the size, shape and orientation of the sample's components.⁴³ The range of q that is typically covered by a SAS instrument is usually around 2×10^{-3} - 0.5 Å^{-1} , which corresponds to 10-3000 Å in real-space. The neutron or X-ray detector of a SAS instrument is often two-dimensional, meaning that for an isotropic scattering profile, the detector image is radially averaged to give an $I(q)$ scattering profile. It is possible to increase the q -range of a SAS instrument through the introduction of wide- q detector banks close to the sample or small- q detector banks further away. This allows the SANS2D instrument, at the ISIS Neutron and Muon Source, to have a total range from 2×10^{-3} - 2 Å^{-1} .⁴⁴ Furthermore, the SANS2D instrument may leverage the ToF method discussed in Section 2.1.2 to allow for a much shorter post sample flight path than is present at D22.

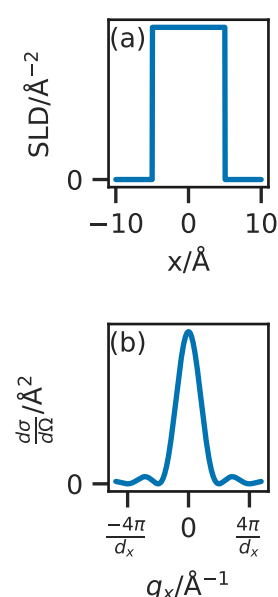
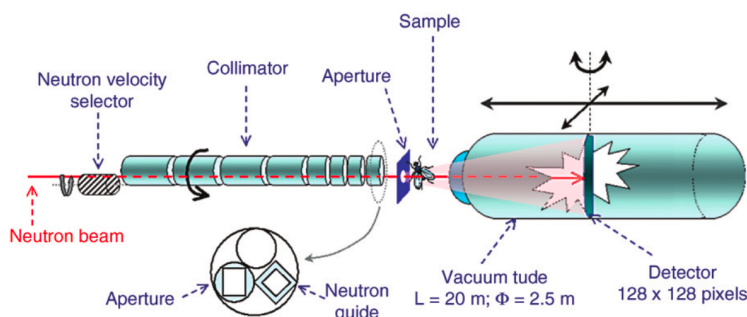


Figure 2.12: The effect of a Fourier transform (a) the scattering length density profile for some object with a width of 10 Å , (b) the Fourier transform of this object showing the minima in the differential cross section at values of $q_x = n\pi/d_x$, where n is some integer. Reprinted with permission of Springer Nature Customer Service Journals from Springer Nature, *Neutron Scattering and Applications in Soft Condensed Matter*, in: *Soft Matter Characterization*, 2018, pp. 189-201 (2018-9-25).



A radially averaged SAS pattern can be considered as consisting of two sections that arise from the form and structure factors for

⁴⁵ K. J. Edler *et al.* *Curr. Opin. Colloid Interface Sci.* 20.4 (2015), pp. 227–234.

the scattering species. The form factor gives information about the average shape of the scattering particle, while the structure factor is a measure of the interaction present between the objects. It is often possible to control the presence of the structure factor by changing the concentration of the sample, eventually, the concentration will be so low that all interparticle interaction is screened by the solvent.⁴⁵ This method is frequently applied in biological SAXS applications, where the interactions between the protein molecules are of less interest than the overall structure of the complex. However, with micelles, it is not always possible to remove the structure factor, as the critical micelle concentration may be higher than the minimum concentration at which the structure factor is present. It is possible to deconvolute the structure and form factors for a micellar solution by studying different concentrations, assuming that the form of the micelle is concentration independent, over the measured concentration range.

The rigorous, model-independent method for the analysis of SAS involves taking the inverse Fourier transform of the scattering profile, to give an auto-correlation function of the average particle in the system, which following a deconvolution procedure will resolve the radially averaged SLD profile. However, this is often cumbersome and has a low information density, when compared to model-dependent techniques. Additionally, if the experimental data lacks information at wide enough q to cover all features of the sample, artefacts may be present in the inverse Fourier transform of the scattering.

There are two common and straight-forward analysis procedures that can be used to give an understanding of the scattering species structure. The first is the Guinier approximation, which is used in the determination of the radius of gyration, R_g , of the scattering species at “infinite dilution”. This scattering law is only valid at very small values of q , where $q < R_g^{-1}$,⁴⁶

⁴⁶ Sivia, *Elementary Scattering Theory: For X-Ray and Neutron Users*, op. cit.

$$\ln[I(q)] = \ln[I(0)] - \left(\frac{R_g^2}{3}\right)q^2. \quad (2.39)$$

This relationship allows the radius of gyration to be found by plotting the scattering profile transformed into $\ln[I(q)]$ vs. q^2 , and evaluating the gradient at low q . The Guinier plot for the scattering from a sphere with a radius of 20 Å is shown in Figure 2.14, where the radius of gyration correlates with the radius of the sphere, R_s , as follows,

$$R_g = \sqrt{\frac{3}{5}}R_s. \quad (2.40)$$

The Guinier analysis is very common in the study of proteins by SAS, as it allows for the determination of the protein size in the native, solution phase.⁴⁷ Another common analysis of SAS data comes in the form of Porod’s law, which states that for large values of q , the scattering intensity becomes proportional to Sq^{-4} , where

⁴⁷ S. Skou *et al.* *Nat. Protoc.* 9.7 (2014), pp. 1727–1739.

S is the surface area of the sample. This means that by plotting $I(q)q^4$ vs. q and extrapolating to $q \rightarrow \infty$, it is possible to determine the external surface area of the system.⁴⁸ Using the surface area, it is then possible to qualitatively determine the “roughness” of the system based on the relation of the surface area to the particle size.

⁴⁸ Willis *et al.*, *Experimental Neutron Scattering*, op. cit.

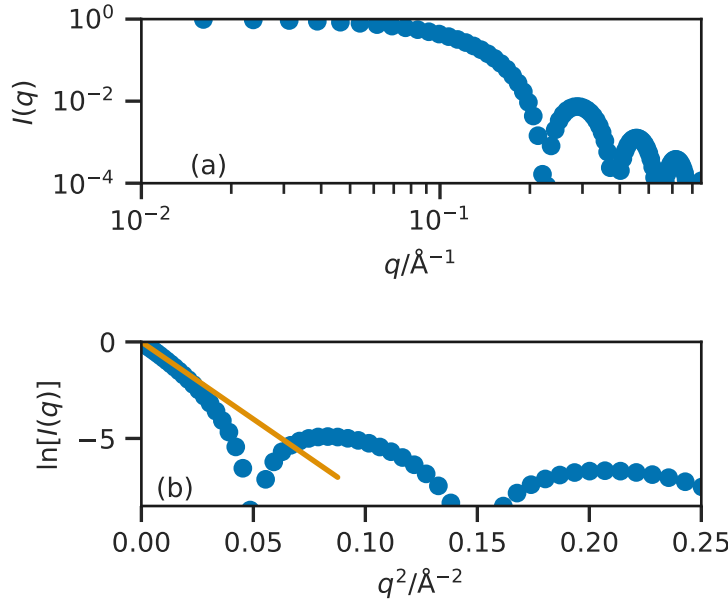


Figure 2.14: The Guinier plot, (a) the ideal scattering profile from a sphere of radius 20 Å, (b) the associated Guinier plot, with a straight line (orange) at low- q showing the radius of gyration to be ~ 15.5 Å.

In the calculation of a SAS pattern, both the structure and form factors will contribute. Therefore, when we model the pattern, the differential cross-section has the following form.⁴⁹

⁴⁹ When the system is centrosymmetric.

$$\frac{d\sigma(q)}{d\Omega} = N_p \Delta SLD^2 V_p^2 P(q) S(q), \quad (2.41)$$

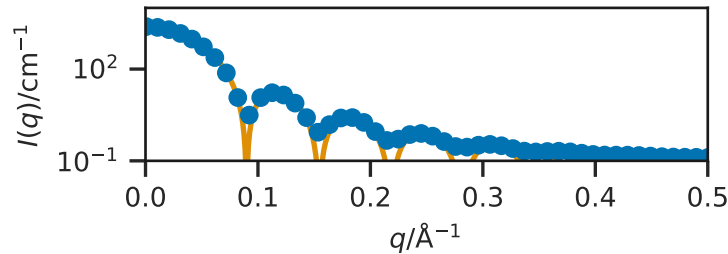
where N_p is the number density of the particles, ΔSLD is the difference in scattering length density between the particles and the solvent, V_p is the particle volume, $P(q)$ is the particle form factor, and $S(q)$ is the structure factor.⁵⁰ Therefore, it is necessary to understand the form and structure factors individually.

⁵⁰ Pedersen, “Monte Carlo Simulation Techniques Applied in the Analysis of Small-Angle Scattering Data from Colloids and Polymer System”, op. cit.

The most common method for the modelling of the form factor is by using very coarse shapes; such as spheres, cylinders, or ellipses. This involves the evaluation of analytical or quasi-analytical solutions for the scattering, which have been derived for many common shapes. The solution for a sphere was solved in the early 19th century by Lord Rayleigh. Pedersen, “Monte Carlo Simulation Techniques Applied in the Analysis of Small-Angle Scattering Data from Colloids and Polymer System”, op. cit.

$$P(q) = \left\{ \frac{3 \{ \sin(qR_s) - qR_s \cos(qR_s) \}}{(qR_s)^3} \right\}^2, \quad (2.42)$$

⁵¹ SASview for Small Angle Scattering. URL: <http://www.sasview.org> (Accessed 2016-10-26); SASfit, URL: [https://kkr.web.psi.ch/sasfit.html](https://kkr.web.psi.ch/sasfit/SASfit.html) (Accessed 2016-10-26), with instrumental smearing) compared with a curve of Equation 2.42, where $R = 50 \text{ \AA}$ (solid line).



where R_s is the radius of the sphere. A comparison between a possible experimental scattering pattern and the scattering generated from Equation 2.42 is shown in Figure 2.15. Analytical form factors exist for a wide variety of shapes; these can be found in software such as SASView and SASFit.⁵¹

The structure factor accounts for the scattering interference that arises from the interaction of different particles. This is modelled using expressions which depend on the nature of the scattering particles; hard-sphere, sticky hard-spheres, screened Coulomb, etc. Structure factor expressions are generated as solutions to the Ornstein-Zernike Equation.⁵² The most relevant structure factor in terms of micelle modelling is probably the Hayter-Penfold Mean Spherical Approximation,⁵³ this is where the micelles are modelled as like-charged, soft spheres and is valid for dilute solutions. Again, a whole range of these structure factor functions are built into the SASView package.⁵⁴

In order to evaluate the scattering profile from an atomic,⁵⁵ it is possible to use the Debye equation.⁵⁶ This is an analytical relationship for the determination of the scattering profile based on the atomic positions, \mathbf{r}_i ,

$$I(q) = \sum_i^N \sum_j^N b_i b_j \frac{\sin(q|\mathbf{r}_i - \mathbf{r}_j|)}{q|\mathbf{r}_i - \mathbf{r}_j|}, \quad (2.43)$$

where, N is the number of particles, q is the scattering vector, and b_i and b_j are the scattering lengths of particles i and j respectively.⁵⁷ The Debye equation is powerful, however, it is not intrinsically parallelisable and scales as $\mathcal{O}(N^2)$. In order to improve the efficiency of the calculation of the scattering profile, a variety of methods have been developed that offer a sufficiently accurate approximation.⁵⁸ The Golden Vector method, developed by Watson and Curtis,⁵⁹ scales as $\mathcal{O}(Nn)$, where n is the number of scattering vectors used in the calculation. In this method, the scattering amplitude is calculated numerically for a single \mathbf{q} -vector,

$$I(\mathbf{q}) = \left[\sum_i^N b_i \cos(\mathbf{q} \cdot \mathbf{r}_i) \right]^2 + \left[\sum_i^N b_i \sin(\mathbf{q} \cdot \mathbf{r}_i) \right]^2. \quad (2.44)$$

⁵² R. Klein. "Interacting Colloidal Suspensions". In: *Neutron, X-Rays and Light. Scattering Methods Applied to Soft Condensed Matter*. 2002, pp. 351–380.

⁵³ J. B. Hayter et al. *Mol. Phys.* 42.1 (1981), pp. 109–118.

⁵⁴ SASview for Small Angle Scattering, op. cit.

⁵⁵ Or any coordinate system, such as a coarse-grained simulation.

⁵⁶ P. Debye. *Ann. Phys.* 351.6 (1915), pp. 809–823.

⁵⁷ In the case of a coarse-grained particle, this can be obtained from summing the scattering lengths of the constituent atoms.

⁵⁸ D. I. Svergun. *Acta Crystallogr. A* 50.3 (1994), pp. 391–402; M. C. Watson et al. *J. Appl. Crystallogr.* 46.4 (2013), pp. 1171–1177.

⁵⁹ Idem, "Rapid and Accurate Calculation of Small-Angle Scattering Profiles Using the Golden Ratio", op. cit.

This is carried out for n scattering vectors that are selected in an orientationally averaged fashion from a quasi-uniform lattice on a sphere. This was first developed such that n is a number from the Fibonacci sequence,⁶⁰ however for the Golden Vector method, n may be any positive integer. This leads to the scattering vectors being calculated as,

$$\begin{aligned} q_x^{(k)} &= q \cos \left[\sin^{-1} \left(\frac{2k}{n} \right) \right] \cos \left(\frac{2\pi k}{\Phi} \right), \\ q_y^{(k)} &= q \cos \left[\sin^{-1} \left(\frac{2k}{n} \right) \right] \sin \left(\frac{2\pi k}{\Phi} \right), \\ q_z^{(k)} &= \frac{2kq}{n}, \end{aligned} \quad (2.45)$$

where, k runs from $-(n-1)/2, \dots, 0, \dots, (n-1)/2$ and Φ is the golden ratio,

$$\Phi = \frac{1 + \sqrt{5}}{2}. \quad (2.46)$$

The approximate orientationally averaged scattering is then found as an average of the scattering from each of their individual q -vectors,

$$I(q) = \frac{1}{n} \left\{ \sum_{k=(1-n)/2}^{(n-1)/2} I[\mathbf{q}^{(k)}] \right\}. \quad (2.47)$$

The accuracy of this calculation increases with n , however agreement, comparable to the Debye equation, between experiment and simulation has been shown for $n < 100$ even for highly anisotropic systems.⁶¹

2.2.8 Contrast variation

The scattering profile generated by the interaction of the chosen system with radiation depends on three factors:

- the spatial arrangement of the atoms in the system,
- the instrument being used to measure the pattern⁶², and
- the interaction between the radiation and the matter under investigation.

This final factor is perhaps better known as the “scattering contrast”, this is an extremely important factor in the study of soft matter, particularly when the probing radiation is the neutron. The scattering contrast makes it possible to select individual components of the system and investigate their structural properties.⁶³ The differential cross-section, $d\sigma/d\Omega$ of a point scatterer, as shown in Equation 2.19, varies only with respect to the scattering length of the species, b ,

$$\frac{d\sigma}{d\Omega} \propto b^2. \quad (2.48)$$

However,⁶⁴ it is often easier to use the SLD.

⁶⁰ Svergun, “Solution Scattering from Biopolymers: Advanced Contrast-Variation Data Analysis”, op. cit.

⁶¹ Watson *et al.*, “Rapid and Accurate Calculation of Small-Angle Scattering Profiles Using the Golden Ratio”, op. cit.

⁶² The instrumental resolution function mentioned in 2.2.5.

⁶³ P. Schurtenberger. “Contrast and Contrast Variation in Neutron, x-Ray and Light Scattering”. In: *Neutron, X-Rays and Light. Scattering Methods Applied to Soft Condensed Matter*. 2002, pp. 145–170.

⁶⁴ As discussed in Section 2.2.4.

⁶⁵ As the X-ray is a form of electromagnetic radiation.

⁶⁶ Leading to variation between isotopes of a given element.

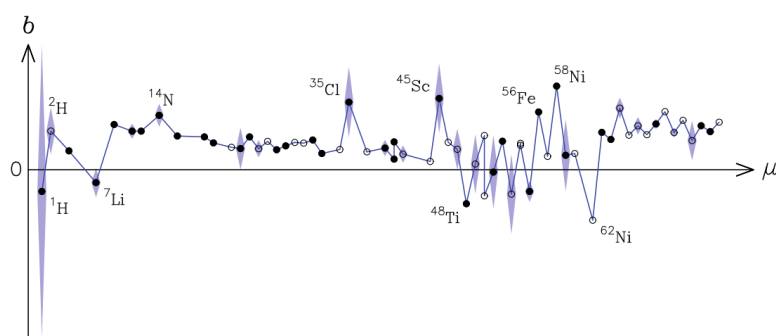
When an X-ray interacts with an atom, it is scattered by the interaction with the electrons.⁶⁵ This means that the scattering length of an atom by an X-ray is directly proportional to the number of electrons in the atom, so it is therefore difficult to discern between the scattering from a carbon atom (6 electrons) and a nitrogen atom (7 electrons). Furthermore, the scattering from hydrogen atoms is practically non-existent, in comparison to heavier elements.

The scattering length from neutrons varies nonsystematically with respect to the atomic number of a species, this is shown in Figure 2.16. In addition to the apparently random variation with changes in atomic number, there is also significant variation with mass number.⁶⁶ There is also dependence due to the magnetic state of the atom, however, this is normally unimportant for soft matter. The scattering lengths differ with the nuclear spin energy level, this leads to an average scattering length, $\langle b \rangle$, for isotopes where the nuclear spin is non-zero. There are two forms of scattering, coherent and incoherent, for which the scattering cross-sections, σ , are determined by,

$$\begin{aligned}\sigma_{\text{coh}} &= 4\pi\langle b \rangle^2 \\ \sigma_{\text{incoh}} &= 4\pi(\langle b^2 \rangle - \langle b \rangle^2)\end{aligned}\quad (2.49)$$

The coherent scattering is the scattering from nuclei that all have the same value of b , and leads to the important scattering pattern. Whereas, the incoherent scattering is caused by the “disorder” between the isotopes, and is the cause of the background present in the measurement. Examples of these scattering cross-sections for nuclei relevant to soft matter are shown in Table 2.2. It can be seen that the incoherent scattering from the ^1H nuclei is more than forty times higher than the coherent scattering. This leads to a large, intrusive background present in the scattering pattern of hydrogenous samples.

Figure 2.16: The variation of the average neutron scattering length, $\langle b \rangle$ (circles), with atomic mass, μ . The standard deviation, Δb , is indicated with the shaded regions. Reproduced, with permission of Oxford University Press, from D. S. Sivia. *Elementary Scattering Theory: For X-Ray and Neutron Users*. 2011.



The difference between the scattering of ^1H and ^2H , evident in Table 2.2, can lead to a very useful technique in soft matter scattering, known as contrast variation. The idea of contrast variation is based on the substitution of one isotope of an atom for another,

while not introducing significant change to the properties of the material. Traditionally the benefit of this came in terms of contrast matching out a part of the system to reduce the dimensionality of the problem for analysis. For example, by matching the solvent SLD to that of the tails of the surfactants at the centre of a micelle, there would only be scattering from the heads, and conversely, there would only be scattering from the tails if the solvent had the same SLD as the head groups. This means that the problem becomes more straightforward as there are fewer variable parameters when fitting the data. This idea is represented graphically in Figure 2.17.

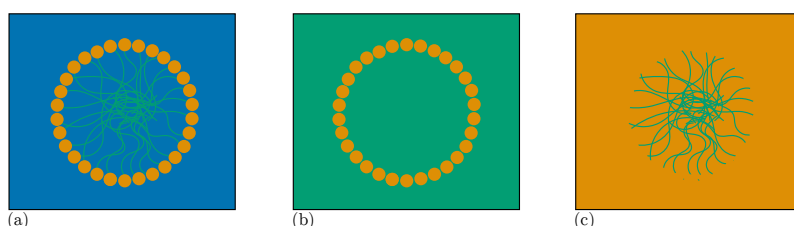


Figure 2.17: The effect of varying the scattering length density of the solvent in a micelle system, (a) the system in a pure solvent, (b) the solvent is contrast matched to the surfactant tails, and (c) the solvent is contrast matched to the surfactant heads.

The technique of contrast variation may also be used in terms of data analysis. By increasing the number of datasets corresponding to a single model at different contrasts, the solution for the true structure of the model from the scattering data becomes more robust. This is due to the fact that each different contrast can be considered as an independent measurement of the same system, and hence each set of scattering data can be used within the data analysis procedure to obtain the best global agreement to the experiment. This co-refinement of multiple experiments can, under the right conditions, be used to simultaneously consider both neutron and X-ray datasets.⁶⁷

There is also the possibility of using contrast variation when the probing radiation is the X-ray, by leveraging anomalous scattering. This is where different wavelengths of radiation give different scattering when the wavelengths are on opposite sides of an X-ray absorption edge. This is not frequently used for soft matter species, as the X-ray absorption edges for elements common in soft matter (H, C, N, O, etc.) are at very low X-ray energies so generally outside of the accessible range of a standard SAXS instrument.⁶⁸

⁶⁷ Nelson, "Co-Refinement of Multiple-Contrast Neutron/X-Ray Reflectivity Data Using MOTOFIT", op. cit.

⁶⁸ Schurtenberger, "Contrast and Contrast Variation in Neutron, x-Ray and Light Scattering", op. cit.

Table 2.2: Examples of coherent and incoherent scattering cross-sections. Reproduced, with permission from Elsevier, from P. Schurtenberger. "Contrast and Contrast Variation in Neutron, x-Ray and Light Scattering". In: *Neutron, X-Rays and Light. Scattering Methods Applied to Soft Condensed Matter*. 2002, pp. 145–170.

Isotope	S	$\sigma_{\text{coh}}/10^{-28} \text{ m}$	$\sigma_{\text{incoh}}/10^{-28} \text{ m}$
^1H	$1/2$	1.8	79.7
^2H	1	5.6	2.0
^{12}C	0	5.6	–
^{14}N	1	11.6	0.3
^{16}O	0	4.2	–

2.3 CLASSICAL SIMULATION

While the currently applied traditional methods for the analysis of experimental scattering data discussed previously are popular. There is growing interest in the use of multi-modal analysis methods that leverage classical simulation to assist in the analysis of scattering data.⁶⁹ This would involve the simulation of the chemical system in order to educate the analysis of the experimental data. These systems, especially when the materials being simulated are soft in nature, are often highly complex and typically cover large length scales. Classical simulation, particularly in combination with coarse-grained potential models, can feasibly enable the simulation of these methods.

In order to simulate a complexity of a real chemical system, it is necessary to model the electrons of the molecules and their interactions. This is usually achieved using quantum mechanical calculations, where the energy of the system is calculated by finding some approximate solution to the Schrödinger equation. However, quantum mechanical calculations are very computationally expensive and are realistically limited to hundreds of atoms. In order to simulate a soft matter system such as a lipid monolayer or polymer nanoparticles, it is necessary to simplify the calculation being performed. This leads to the use of classical simulations, where parameterised analytical functions are used to represent the potential energy of the system. Classical simulations are used substantially in this work, in terms of molecular dynamics simulations.⁷⁰ Therefore, it is necessary to introduce the underlying theory on which this method is defined.

2.3.1 Potential models

Potential modelling is a more computationally efficient method for the calculation of the potential energy of a chemical system. A potential model consists of a series of mathematical functions that depend on the atomic positions, \mathbf{r} . Each of the functions represents the potential energy of a different interaction for a given atom. Broadly, these interactions can be split into bonded and non-bonded, such that the total energy may be described as follows,

$$E_{\text{total}}(\mathbf{r}) = \sum_{\text{bonded pairs}} E_{\text{bonded}}(\mathbf{r}) + \sum_{\text{atom pairs}} E_{\text{non-bonded}}(\mathbf{r}). \quad (2.50)$$

The total potential energy is then the sum of the potential energy for each of the individual atoms.

The bonded terms are used to describe different aspects of chemical bonds. These typically consist of bond stretches, angle bends and dihedral torsions, these interactions have the following mathematical form,⁷¹

⁶⁹ Ivanović *et al.*, "Temperature-Dependent Atomic Models of Detergent Micelles Refined against Small-Angle X-Ray Scattering Data", *op. cit.*; Scoppola *et al.*, "Combining Scattering and Computer Simulation for the Study of Biomolecular Soft Interfaces", *op. cit.*; Dabkowska *et al.*, "Modulation of Dipalmitoylphosphatidylcholine Monolayers by Dimethyl Sulfoxide", *op. cit.*; J. S. Hub. *Curr. Opin. Struct. Biol.* 49 (2018), pp. 18–26.

⁷⁰ Molecular dynamics (MD) is discussed in detail in Section 2.4.

⁷¹ These forms are specific to the OPLS2005 potential model (J. L. Banks *et al. J. Comput. Chem.* 26.16 (2005), pp. 1752–1780), other potential models may have different functions.

$$\begin{aligned}
E_{\text{bonded}}(b, \theta, \phi) = & \sum_{\text{bonds}} K_b(b - b_0)^2 + \sum_{\text{angles}} K_\theta(\theta - \theta_0)^2 \\
& + \sum_{\text{dihedrals}} \frac{1}{2} \{ A_1[1 + \cos(\phi)] \\
& + A_2[1 - \cos(2\phi)] + A_3[1 + \cos(3\phi)] \},
\end{aligned} \tag{2.51}$$

where, K_b and b_0 , K_θ , θ_0 , and A_1 , A_2 , and A_3 are interaction dependent parameters for the bonds, angles, and dihedrals respectively, while b , θ , and ϕ are the bond lengths, the size of the angles, and the size of the dihedrals that depend on the atom positions.⁷² It can be seen that both the bond stretch and angle bend have harmonic functions, whereas the dihedral consists of a more complex multiple cosine functions.

The non-bonded terms are a series of functions that describe the potential energy of intermolecular interactions, such as electrostatics and London dispersion forces. The potential energies of the short-range interactions are usually modelled as a combination of the attractive London dispersion interaction and the repulsive exchange forces that arise from the Pauli exclusions principle.⁷³ These are often forms such as shown below for the Lennard-Jones potential model,⁷⁴

$$\begin{aligned}
E_{\text{non-bonded}}(r) = & E_{\text{repulsive}} + E_{\text{attractive}} \\
= & \frac{A}{r^{12}} - \frac{B}{r^6} = 4\epsilon \left[\left(\frac{\sigma}{r} \right)^{12} - \left(\frac{\sigma}{r} \right)^6 \right]
\end{aligned} \tag{2.52}$$

where, r is the distance between two particles, A and B are interaction dependent parameters, and σ and ϵ are simple reformations of these parameters,

$$A = 4\epsilon\sigma^{12} \quad B = 4\epsilon\sigma^6. \tag{2.53}$$

Figure 2.18 shows each component of the Lennard-Jones potential model for atoms of argon.⁷⁵ The Lennard-Jones potential model is not the only form that may be used for the modelling of the short-range non-bonded interactions, others such as the Buckingham and Morse potentials exist.⁷⁶ In each case, there is a short ranged repulsive interaction to describe the electrostatic repulsion between the electron clouds, and a longer range attractive component that represents dispersion interactions. However, the Lennard-Jones model has been used heavily in this work.

While the short-range interactions can be accounted for by a function such as the Lennard-Jones potential model, the potential energy of the long-range electrostatic interactions are usually modelled, more consistently, using Coulomb's law for classical electrostatic interaction between point particles,⁷⁷

$$E_{\text{Coulomb}}(r) = \frac{1}{4\pi\epsilon_0} \frac{q_i q_j e^2}{r^2}, \tag{2.54}$$

where, r is the distance between the two particles, ϵ_0 is the dielectric permittivity of the vacuum, e is the charge of the electron, and

⁷² The values for the interaction dependent parameters are determined as outlined in Section 2.3.2.

⁷³ A. R. Leach. *Molecular Modelling: Principles and Applications*. 1996.

⁷⁴ J. E. Lennard-Jones. *Proc. Royal Soc. Lond. A*. 106.738 (1924), pp. 463–477.

⁷⁵ Using parameters for A and B determined in A. Rahman. *Phys. Rev.* 136 (2A 1964), A405–A411.

⁷⁶ R. A. Buckingham. *Proc. Royal Soc. Lond. A*. 168.933 (1938), pp. 264–283; P. M. Morse. *Phys. Rev.* 34.1 (1929), pp. 57–64.

⁷⁷ C. A. Coulomb. *Histoire de l'Académie Royale des Sciences*. Imprimerie Royale (1788), pp. 569–577; C. A. Coulomb. *Histoire de l'Académie Royale des Sciences*. Imprimerie Royale (1788), pp. 578–611.

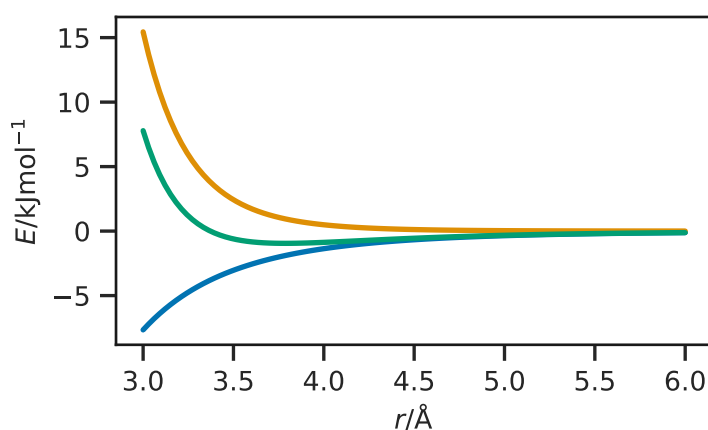


Figure 2.18: The form of each component; attractive (blue), repulsive (orange), of the Lennard-Jones potential model (green) for argon, using parameters in A. Rahman. *Phys. Rev.* 136 (2A 1964), A405–A411.

q_i and q_j are the electronic charges on each of the particles. It is clear that when q_i and q_j have the opposite signs Coulomb's law is always attractive. The fact that Equation 2.54 contains a factor of r^{-2} indicates that this is a much longer range interaction than those modeled with the Lennard-Jones model, make the Coulomb potential more complex to compute.⁷⁸

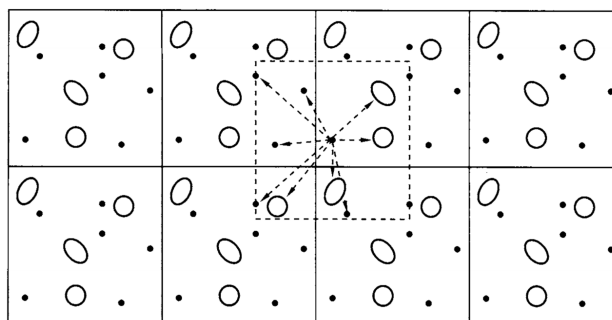
An example of a very large classical simulation would be ~ 3 million atoms.⁷⁹ However, this is still only 1.8×10^{-16} mol which is not remotely realistic as a simulation of a “real” system. A common method to allow for the apparent simulation of a much larger system is the use of periodic boundary conditions.⁸⁰ This is where a boundary condition is applied to the edges of the simulation cell, such as to mimic an infinite system, such that the simulation cell is surrounded by identical images of itself, this is shown pictorially in Figure 2.19. Using the PBC means that atomic diffusion is conserved as when an atom reaches the edge of the simulation cell, it will appear on the other side as though it came from the adjacent periodic cell. The use of a periodic boundary condition is particularly powerful in the simulation of homogenous systems, such as liquids.

⁷⁸ D. Frenkel *et al.* *Understanding Molecular Simulation: From Algorithms to Applications*. 1996.

⁷⁹ J. Gumbart *et al.* *Structure* 17.11 (2009), pp. 1453–1464.

⁸⁰ Abbreviated to PBC.

Figure 2.19: A graphical representation of the periodic boundary conditions. Reprinted, with permission of Elsevier, from D. Frenkel *et al.* *Understanding Molecular Simulation: From Algorithms to Applications*. 1996.



The cut-off is another important factor for classical simulation,

this is the distance after which the energy between two particles is considered to be zeros. Therefore, for distances greater than the cut-off, it is not necessary to calculate the energy between the two particles as it is taken to be zero.⁸¹ Code Block 2.2 gives an example of some code that could be used to calculate the Lennard-Jones energy of an atomistic system, where both the periodic boundary condition and the energy cut-off distance are considered.

⁸¹ This leads to an increase in the computational efficiency.

```
import numpy as np

def lj_energy(coordinates, cell, cut_off, A, B):
    """
    Calculates the potential energy arising from the Lennard-Jones
    potential model from a series of atomistic particles.

    Parameters
    -----
    coordinates: float, array-like (N, 3)
        An array of the x, y, and z coordinates for each of the N
        particles in the simulation.
    cell: float, array-like
        An array of length 3 containing the simulation cell vectors.
    cut_off: float
        The potential energy cut_off value for the simulation.
    A: float
        The A parameter in the Lennard-Jones potential model.
    B: float
        The B parameter in the Lennard-Jones potential model.

    Returns
    -----
    float, array-like
        An array of length N containing the energy of each particle
        in the simulation.
    """
    energy = np.zeros((coordinates.shape[0]))
    for i in range(coordinates.shape[0] - 1):
        for j in range(i + 1, coordinates.shape[0]):
            d = coordinates[j] - coordinates[i]
            d = d % cell
            r = np.sqrt(np.sum(np.square(d)))
            if r > cut_off:
                continue
            else:
                energy[i] += A / np.power(r, 12) - B / np.power(r, 6)
                energy[j] += A / np.power(r, 12) - B / np.power(r, 6)
    return energy
```

Code Block 2.2: Code that may be used to generate the Lennard-Jones energy for a given atomistic system, which accounts for the periodic boundary condition and the energy cut-off distance.

The use of the PBC may be problematic for systems containing long-range interactions, such as classical electrostatics, due to the fact that the range of the electrostatic interaction may be much greater than the size of half of the simulation cell, which can be taken to be the energy cut-off distance. In order to avoid truncation artefacts, the Ewald summation is often used for the calculation of the electrostatic contribution to the potential energy.⁸² The Ewald summation involves performing the summation of the contributing interaction energies in reciprocal space rather than in real space as is the case for the short-range interactions. Most modern molecular dynamics simulation software packages implement the Ewald summation using a particle mesh Ewald (PME) method.⁸³

⁸² P. P. Ewald. *Ann. Phys.* 369.3 (1921), pp. 253–287.

⁸³ U. Essmann *et al.* *J. Chem. Phys.* 103.19 (1995), pp. 8577–8593.

2.3.2 Parameterisation

Section 2.3.1 introduced the idea of potential models that may be used to evaluate the potential energy of a given system, requiring much less time than methods that rely on the use of quantum mechanics. However, for these methods to be effective, it is important that the potential models used are able to model the system under study accurately. This is achieved initially by selecting the correct

potential model for a given interaction, and then by ensuring that the interaction-dependent parameters are accurate for a given interaction. The method of obtaining such parameters is referred to as “parameterising” the model. Model parameterisation is important for all types of potential models, for example it is necessary to determine the equilibrium bond length b_0 and the force constant K_b for a given covalent bonds, or the partial electrostatic charge that is present on a carbonyl oxygen atom when it interacts with the hydrogen atom from a neighbouring hydroxyl group.

Parameterisation of a potential model is usually achieved by fitting the potential model functions to energetic data obtained using a higher accuracy technique.⁸⁴ We will not dwell on the details of potential model parameterisation,⁸⁵ however, it is important to note that the parameters used in MD simulation are not absolute and depend heavily on the merits of the parameterisation method.

In this work, we have focused heavily on the use of off-the-shelf potential models, to ensure the easy replicability of the work. Off-the-shelf potential models are those that are determined to be applied to a wide range of chemical systems. An example includes the OPLS potential model which was parameterised by comparison to quantum mechanical measurements and crystallographic data.⁸⁶ While these off-the-shelf potential models are useful for their ease-of-use, it is noted that often these forcefields may require optimisation for the particular system.

⁸⁴ These may be quantum mechanical calculations or experimental methods.

⁸⁵ This is discussed in detail in many textbooks such as J. Harvey. *Computational Chemistry*. 2018; Leach, *Molecular Modelling: Principles and Applications*, op. cit.

⁸⁶ W. L. Jorgensen *et al.* *J. Am. Chem. Soc.* 110.6 (1988), pp. 1657–1666.

2.3.3 Coarse-graining

The atomistic simulation of very large systems, such as multiple surfactant micelles or large lipid monolayers, require a huge number of atoms. While computational efficiency improvements such as the PBC or the energy cut-off distance are able to reduce the time taken to simulate these systems, it is often still not possible to produce physically meaningful simulations,⁸⁷ without including some other efficiency improvements.

This has led to the use of coarse-graining of molecules in simulations. This is the definition of super-atoms, in the place of groups of atoms, known as “beading”, some examples are shown for the MARTINI force field⁸⁸ in Figure 2.20. Each of the super-atoms must correspond to the chemistry of the underlying atoms. For example the MARTINI potential model, introduces five different apolar, beads to represent the polarity of the carbon atoms that make up the super-atom. Additionally, there are thirteen other super-atom types that can be used to model polar, nonpolar, and charged atomic groups.

In addition to the computational benefit of having fewer particles in the simulation,⁸⁹ there is also the opportunity to increase the timestep length for the simulation.⁹⁰ This can be achieved as the highest frequency vibrations that must be modelled in the sys-

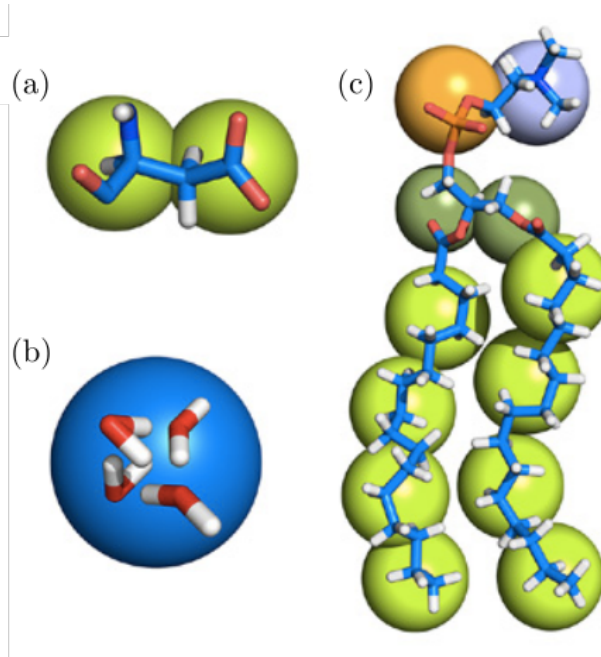
⁸⁷ In particular for emergent properties that depend on large system sizes and long simulation times.

⁸⁸ Marrink *et al.*, “The MARTINI Force Field: Coarse Grained Model for Biomolecular Simulations”, op. cit.

⁸⁹ Therefore requiring fewer integrations of the equations of motion

⁹⁰ K. Pluhackova *et al.* *J. Phys. Condens. Matter* 27.32 (2015), p. 323103.

Figure 2.20: Three examples of the MARTINI coarse-graining mechanism for (a) aspartic acid, (b) a water cluster, and (c) a molecule of DPPC. Reprinted with permission of the Institute of Physics, from K. Pluhackova *et al.* *J. Phys. Condens. Matter* 27.32 (2015), p. 323103.



tem are integrated out. For example, another coarse-grained model called the united atom potential model, where the hydrogen atoms have been integrated out, the time step may be larger than for the same all-atom system as it is no longer necessary to model the high-frequency C–H bond.

The technique of coarse-graining a molecule can range from the integration of the hydrogen atoms into the heavier atoms to which they are bound, all the way to the treatment of entire molecules as a single “bead”, with the inclusion of an implicit solvent. The parameterisation of a coarse-grained potential model is carried out in much the same way as discussed in Section 2.3.2 for all-atom potential models. The coarse-grained parameters are determined by comparison with a higher-resolution technique.⁹¹

⁹¹ Often this is all-atom molecular dynamics simulations.

2.4 OPTIMISATION & SAMPLING METHODS

In this work, computational modelling methods have been applied to important scattering problems. The aim of many modelling problems is to optimise a series of parameters such that a minimum in some parameter-dependent metric is found. While, in other circumstances, the aim is to sample the parametric search-space of a particular problem. The problem of parameter optimisation and sampling is a massive area of mathematics and computer science and is it not possible to introduce the whole field. Therefore, I will introduce two optimisation methods and two sampling methods that are applied within this work.

Both optimisation algorithms in this work are population-based, making use of a population of candidate solutions. These populations of candidate solutions often have knowledge of the state

⁹² G. Wu *et al.* *Swarm Evol. Comput.* 44 (2019), pp. 695–711.

⁹³ Wormington *et al.*, “Characterization of Structures from X-Ray Scattering Data Using Genetic Algorithms”, op. cit.

⁹⁴ Björck, “Fitting with Differential Evolution: An Introduction and Evaluation”, op. cit.; M. Björck *et al.* *J. Appl. Crystallogr.* 40.6 (2007), pp. 1174–1178; Nelson, “Co-Refinement of Multiple-Contrast Neutron/X-Ray Reflectivity Data Using MOTOFIT”, op. cit.; Nelson *et al.*, “Refnx: Neutron and X-Ray Reflectometry Analysis in Python”, op. cit.; F. Ott. *SimulReflec*. URL: <http://www-llb.cea.fr/prism/programs/simulreflec/simulreflec.html> (Accessed 2019-3-4); P. A. Kienzle *et al.* *NCNR Reflectometry Software*. URL: <http://www.ncnr.nist.gov/reflpak> (Accessed 2018-3-4).

⁹⁵ Storn *et al.*, “Differential Evolution – A Simple and Efficient Heuristic for Global Optimization over Continuous Spaces”, op. cit.

⁹⁶ J. H. Holland. *Adaptation in Natural and Artificial Systems*. 1992.

⁹⁷ Many of these exist however we will discuss a simple classical trial method, details of other methods may be found in Björck, “Fitting with Differential Evolution: An Introduction and Evaluation”, op. cit.

of each other through some interaction method. The interaction method is often used to characterise the algorithms, into evolutionary algorithms and swarm intelligence algorithms.⁹² These population methods are usually more efficient at finding the global minimum for a given search space, than a single candidate method.

2.4.1 Differential evolution

Differential evolution (DE) is a common, iterative optimisation algorithm, that was first applied to the analysis of reflectometry and diffraction data by Wormington *et al.*⁹³ Since then, it has proven very popular for the optimisation of reflectometry data and is included in many common analysis programs.⁹⁴ The DE algorithm is designed to more ably determine the global minimum of a particular function.⁹⁵

DE is an example of a genetic algorithm, one that is designed to mimic the evolution processes observed in biology.⁹⁶ The method consists of two vectors, the parent population, \mathbf{p} , the offspring population, \mathbf{o} . These vectors are of a dimension $(i \times j)$, where i is the number of variables being optimised and j is the number of candidate solutions being used. The offspring population vector is created through some trial methods.⁹⁷

A classical trial method consists of two stages, mutation and recombination. The mutation stage involves performing some mutation on the parent population to create a mutant vector, \mathbf{m} , analogous to the mutation in biological evolutionary theory. The magnitude of the mutation is dependent on the mutation constant, k_m ,

$$\mathbf{m}_{i,j} = b_i + k_m(\mathbf{p}_{i,R1} - \mathbf{p}_{i,R2}), \quad (2.55)$$

where b_i is the best candidate solution in the parent population, and $\mathbf{p}_{i,R1}$ and $\mathbf{p}_{i,R2}$ are randomly chosen members of the parent population. The mutation constant can be considered as a control variable for the size of the search radius, with a large k_m corresponding to a larger search radius.

The recombination step creates the offspring population vector by taking a sample from either the parent population or mutant vectors with some frequency, which depends on the recombination constant, k_r ,

$$\mathbf{o}_{i,j} = \begin{cases} \mathbf{m}_{i,j}, & \text{where } X < k_r \\ \mathbf{p}_{i,j}, & \text{otherwise} \end{cases} \quad (2.56)$$

where, $X \sim U[0, 1)$. The recombination constant controls the progress of the algorithm as it impacts the frequency with which mutation is introduced into the offspring population vector.

The final stage is to compare the offspring and parent population vectors, in the selection stage to create the new parent population for the next iteration. The selection stage comprises of using some figure of merit, ζ , to choose between the subunit from the

offspring or parent population vector. In our example, that figure of merit may be the agreement between some experimental data and our model, or for the example in Figure 2.21 it is the value of the Ackley function,⁹⁸ which we are trying to minimise.⁹⁹

$$\mathbf{p}_{*,j} \leftarrow \begin{cases} \mathbf{o}_{*,j}, & \text{where } \zeta_{\mathbf{o}_{*,j}} < \zeta_{\mathbf{p}_{*,j}} \\ \mathbf{p}_{*,j}, & \text{otherwise} \end{cases} \quad (2.57)$$

where, the * notation indicates all objects in the given population, and $\zeta_{\mathbf{o}_{*,j}}$ and $\zeta_{\mathbf{p}_{*,j}}$ are the figures of merit for the offspring and population candidate solutions respectively.

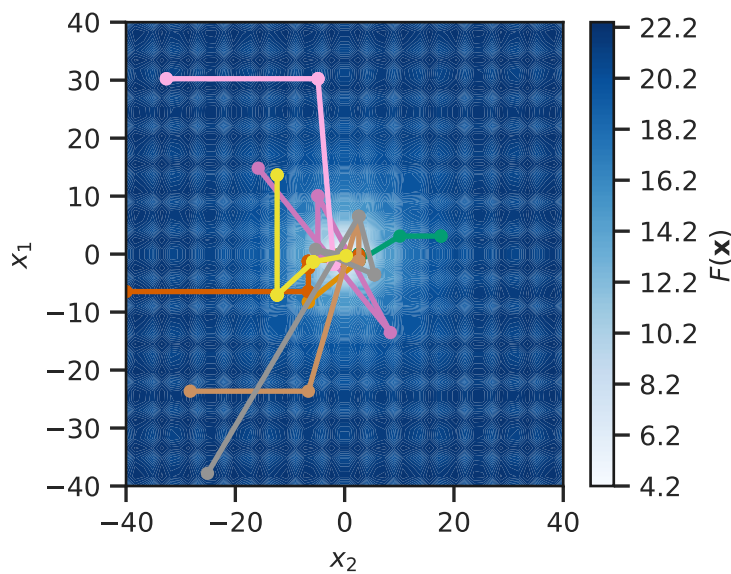


Figure 2.21: An example of a differential evolution (DE) algorithm as applied to an Ackley function, where $\alpha = 20$, $b = 0.2$, and $c = 2\pi$. The mutation and recombination constant in this implementation are both 0.5. Each different coloured line represents a different candidate solution. The optimisation was stopped after 100 iterations had run.

It is noted that it is often the case,¹⁰⁰ that there should be some bounds applied to the variables within the populations. However, the DE algorithm may disregard these bounds due to the nature of the mutation step. Therefore, it is common in DE algorithms, where bounds must be set, that if the search space moves outside that expected it is necessary to reinitialise the parameter. An implementation of the DE algorithm is given programmatically in Code Block 2.3,¹⁰¹ where this reinitialisation is achieved by obtaining a new random number within the given bounds.

¹⁰⁰ In particular for the optimisation of experimental data.

¹⁰¹ Additional Code Blocks showing the mutation, recombination, selection steps may be found in Appendix A.

2.4.2 Particle swarm

Particle swarm optimisation¹⁰² is a type of swarm intelligence population-based optimisation method. This optimisation method was originally developed by Kennedy, Eberhart, and Shi.¹⁰³ Particle swarm methods are particularly suitable for the optimisation, and sampling, of parametric search-spaces with a large number of

¹⁰² Abbreviated to PSO.

¹⁰³ Kennedy *et al.*, "Particle Swarm Optimization", op. cit.; Shi *et al.*, "A Modified Particle Swarm Optimizer", op. cit., The initial purpose of the algorithm was to simulate social organisms such as bird flocks.

```

import numpy as np
import mutation as mut
import recombination as recomb
import selection as sel

def differential_evolution(
    population, f, km, kr, bounds, stop, max_iter
):
    """
    An implementation of a differential evolution algorithm.

    Parameters
    -----
    population: float, array_like
        The initial parent population vector. An array of
        shape (i, j), where i is the number of variables and
        j is the population size.
    f: function
        The figure of merit function to be minimised.
    km: float
        The mutation constant.
    kr: float
        The recombination constant.
    bounds: float, array_like
        The minimum and maximum values for the bounds.
    stop: float
        The value at which the optimisation should stop.
    max_iter: int
        The maximum number of iterations that should be performed
        regardless of if stop is reached.

    Returns
    -----
    float, array_like
        The history of the parameters being fit. An array of
        shape (m, n, j), where n is the number of iterations,
        m is the number of parameters, and j is the population
        size.
    """
    history = np.array([population])
    best = population[:, np.argmin(f(population))]
    i = 0
    while f(best) > stop and i < max_iter:
        mutant = mut.mutation(population, best, km)
        offspring = recomb.recombination(population, mutant, kr)
        offspring[
            np.where(offspring >= bounds[1])
            or np.where(offspring < bounds[0])
        ] = np.random.uniform(bounds[0], bounds[1], 1)
        selected = sel.selection(population, offspring, f)
        history = np.append(history, selected)
        history = np.reshape(
            history, (i + 2, population.shape[0], population.shape[1])
        )
        population = np.array(selected)
        best = population[:, np.argmin(f(population))]
        i += 1
    return history

```

Code Block 2.3: An example of a simple implementation for a DE algorithm as described in M. Björck. *J. Appl. Crystallogr.* 44.6 (2011), pp. 1198–1204.

similar minima. Therefore, I believe that it will be useful for the study of the self-assembly of soft matter materials.¹⁰⁴

These methods consist of a population vector, similar to that described for the differential evolution, that moves around the parametric search-space. The motions of these “particles” are influenced by the positions of the other particles in the vector.¹⁰⁵ It is anticipated that this will lead the swarm to optimise the function under investigation.

Particles in the swarm are under the influence of two elastic forces. The first attracts the particle to the best location in the search-space that the particular particle has found, while the other attracts the particle to the best search-space location found by any particle of the swarm. The magnitudes of these forces are randomised but modulated by a pair of acceleration coefficients; ψ_p that influences the attraction towards the personal best location and ψ_g that influences the attraction to the global best location. The position of a particle changes between iterations of the algorithm based on the following relation,

$$\mathbf{p}_{*,j} \leftarrow \mathbf{p}_{*,j} + \mathbf{v}_{*,j}, \quad (2.58)$$

where, $\mathbf{p}_{*,j}$ is the position of the particle, and $\mathbf{v}_{*,j}$ is the velocity of the particle. This velocity is determined as shown below,

$$\mathbf{v}_{*,j} \leftarrow \omega \mathbf{v}_{*,j} + \psi_g R1(\mathbf{g}_* - \mathbf{p}_{*,j}) + \psi_p R2(\mathbf{s}_{*,j} - \mathbf{p}_{*,j}), \quad (2.59)$$

where, ω a constant known as the inertia weight, $R1 \sim U[0, 1)$ and $R2 \sim U[0, 1)$ are random numbers, \mathbf{g}_* is the best position occupied by any particle in the swarm and $\mathbf{s}_{*,j}$ is the personal best for the particle j .

Figure 2.22 shows an example of the particle swarm optimisation in action, applied to the Ackley function.¹⁰⁶ Code Block 2.4 shows a functional programmatic implementation of a particle swarm optimisation algorithm.

2.4.3 Markov chain Monte-Carlo

Markov chain Monte Carlo¹⁰⁷ is a sampling methodology, derived from direct sampling Monte-Carlo.¹⁰⁸ The aim of an MCMC algorithm is to sample a probability distribution, when parameters are described in terms of their degree of probability.¹⁰⁹ Similar to MD, in practical terms, MCMC should not be used on a system that is not already optimised, as its purpose is probability distribution sampling rather than minimisation. Generally, the approach would be to optimise using, for example, one of the approaches described above, then to use MCMC or molecular dynamics to sample the appropriate search-space. For example, in this work MCMC is used following the optimisation of a reflectometry model using a differential evolution algorithm, to quantify the inverse uncertainties of the model.¹¹⁰ In addition to being able to give information

¹⁰⁴ This is the focus of Chapter ??.

¹⁰⁵ Poli, “Analysis of the Publications on the Applications of Particle Swarm Optimisation”, op. cit.

¹⁰⁶ Ackley, “A Connectionist Machine for Genetic Hillclimbing”, op. cit.

¹⁰⁷ Abbreviated to MCMC.

¹⁰⁸ W. Krauth. *Statistical Mechanics: Algorithms and Computations*. Oxford Master Series in Statistical, Computational, and Theoretical Physics 13. 2006.

¹⁰⁹ D. S. Sivia *et al.* *Data Analysis: A Bayesian Tutorial*. 2006.

¹¹⁰ This is the name given to the uncertainties in the parameters fitted in the modelling process.

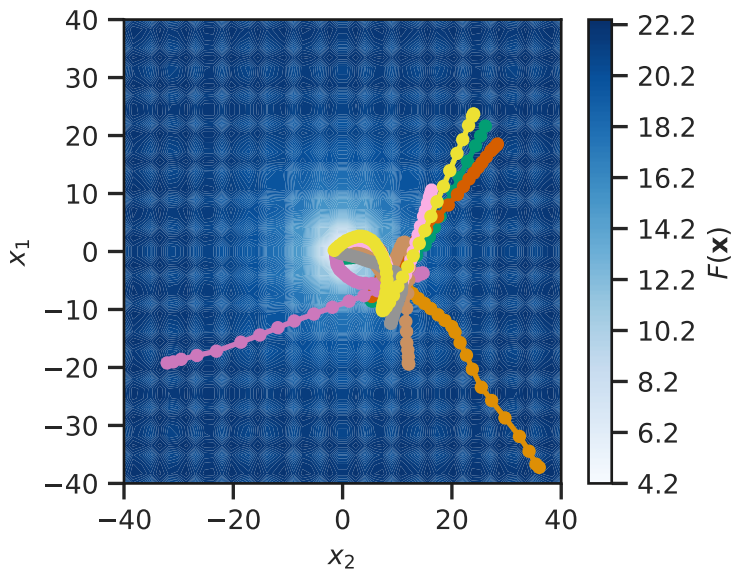


Figure 2.22: An example of a particle swarm optimisation as applied to an Ackley function, where $a = 20$, $b = 0.2$, and $c = 2\pi$. For the particle swarm, the following parameters were used $\omega = 0.9$, $\psi_g = 0.05$, and $\psi_p = 0.05$. Each different coloured line represents a different candidate solution. The optimisation was stopped after 100 iterations had run.

```
import numpy as np

def particle_swarm(position, f, omega, psig, psip, stop, max_iter):
    """
    An implementation of a particle swarm optimisation algorithm.

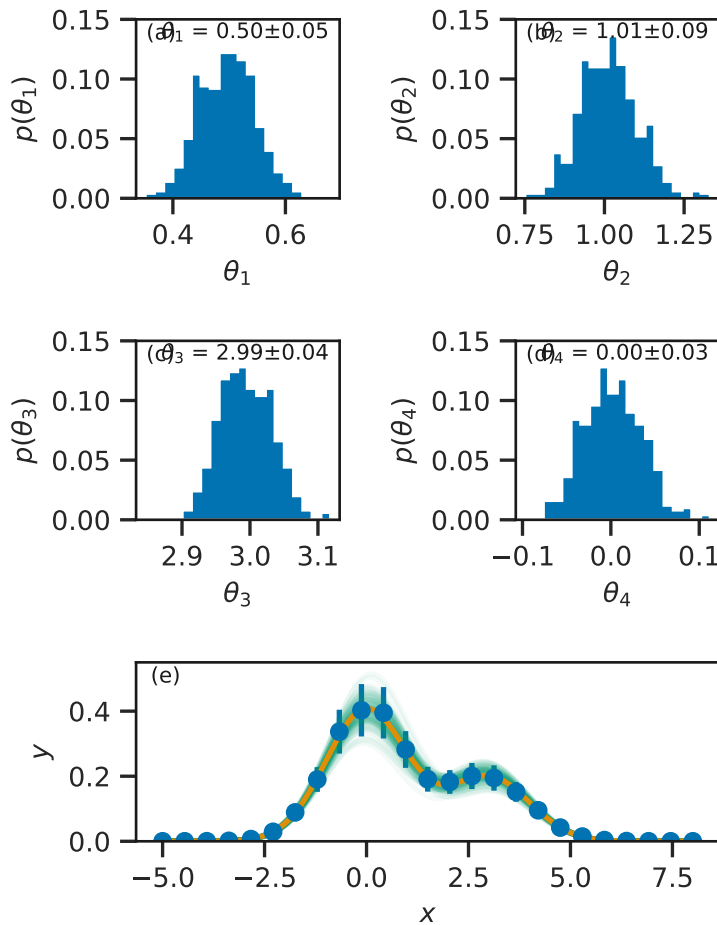
    Parameters
    -----
    position: float, array_like
        The initial position vector. An array of shape (i, j),
        where i is the number of variables and j is the
        population size.
    f: function
        The figure of merit function to be minimised.
    omega: float
        The inertia weight.
    psig: float
        The global acceleration coefficient.
    psip: float
        The personal acceleration coefficient.
    stop: float
        The value at which the optimisation should stop.
    max_iter: int
        The maximum number of iterations that should be performed
        regardless of if stop is reached.

    Returns
    -----
    float, array_like
        The history of the parameters being fit. An array of
        shape (m, n, j), where n is the number of iterations,
        m is the number of parameters, and j is the population
        size.
    """
    history = np.array([position])
    velocity = np.zeros_like(position)
    g_best = position[:, np.argmin(f(position))]
    p_best = np.array(position)
    i = 0
    while f(g_best) > stop and i < max_iter:
        for j in range(velocity.shape[1]):
            velocity[:, j] = (
                omega * velocity[:, j]
                + psig * np.random.rand() * (g_best - position[:, j])
                + psip
                * np.random.rand()
                * (p_best[:, j] - position[:, j])
            )
            position[:, j] = position[:, j] + velocity[:, j]
            history = np.append(history, position)
            history = history.reshape(
                history, (i + 2, position.shape[0], position.shape[1])
            )
        test_g_best = position[:, np.argmin(f(position))]
        if f(test_g_best) < f(g_best):
            g_best = test_g_best
        test_p_best = np.array(position)
        for j in range(position.shape[1]):
            if f(test_p_best[:, j]) < f(p_best[:, j]):
                p_best[:, j] = test_p_best[:, j]
        i += 1
    return history
```

Code Block 2.4: An example of the particle swarm optimisation algorithm from R. Poli. *J. Artif. Evol. Appl.* 2008 (2008), pp. 1–10.

about the inverse uncertainties, MCMC also offers a more complete understanding of the correlations present between the different parameters,¹¹¹ as the interactions between the parameter variation has been quantified.

The aim of MCMC is to only sample configurations of a given function that are within the experimental uncertainty. Figure 2.23 shows an example of the possible output that may be obtained from the application of an MCMC sampling method. This was generated using a Metropolis-Hastings MCMC algorithm,¹¹² shown in Code Block ?? . Initially, a Levenberg–Marquardt algorithm¹¹³ was used to optimise the positions and integral of the two Gaussian functions that make up the data. The MCMC was used to sample the values that were within the experimental uncertainty.



Once an optimised solution, θ , is obtained, the figure of merit is calculated, in Code Block ?? this is the agreement between the model and the experimental data, χ^2 , where,

$$\chi^2 = \sum \frac{(y_{\text{exp}} - y_{\text{calc}})^2}{dy_{\text{exp}}}, \quad (2.60)$$

¹¹¹ W. Gilks *et al.* *Markov Chain Monte Carlo in Practice*. Chapman & Hall/CRC Interdisciplinary Statistics. 1995.

¹¹² Metropolis *et al.*, "Equation of State Calculations by Fast Computing Machines", *op. cit.*; Hastings, "Monte Carlo Sampling Methods Using Markov Chains and Their Applications", *op. cit.*

¹¹³ K. Levenberg. *Quart. Appl. Math.* 2.2 (1944), pp. 164–168; D. W. Marquardt. *J. Soc. Indust. Appl. Math.* 11.2 (1963), pp. 431–441.

Figure 2.23: An example of a four variable (two nearby Gaussian functions of different sizes with added random noise and some fractional uncertainty) problem probed using a MCMC method, using values of $a = 0.1$, θ_1 and θ_2 correspond to the integral of the Gaussian function, while θ_3 and θ_4 indicate their positions; (a)–(d) histograms of the probability distribution function for each of the variables, and (e) the data (blue circles), the optimised solution (orange line), and a series of probable solutions (green lines) showing the variability present in the data uncertainty.

Code Block 2.5: An example of the Metropolis-Hastings MCMC algorithm N. Metropolis *et al.* *J. Chem. Phys.* 21.6 (1953), pp. 1087–1092; W. K. Hastings. *Biometrika* 57.1 (1970), pp. 97–109.

```
import numpy as np

def mcmc(theta, f, a, data, iterations, nburn):
    """
    A simple implementation of the Metropolis-Hasting MCMC algorithm

    Parameters
    -----
    theta: float, array_like
        Initial values for the variables. An array of length n,
        where n is the number of variables.
    f: function
        The function being fit to the data.
    a: float, array_like
        The step size. An array of length n, where n is the number
        of variables.
    data: float, array_like
        The data being assessed. An array of shape (m, 3)
        containing x, y, and dy.
    iterations: int
        The number of accepted iterations to obtain.
    nburn: int
        The number of accepted iterations to ignore during the
        burn-in phase.

    Returns
    -----
    float, array_like
        The history of the parameters being fit. An array of
        shape (m, n), where n is the number of iterations,
        and m is the number of parameters.
    """
    accepted = np.array([])
    calc_y = f(data[0], theta)
    chi2 = np.sum(np.square((data[1] - calc_y) / data[2]))
    i = 0
    while i < iterations:
        new_theta = theta + a * np.random.randn(theta.size)
        new_calc_y = f(data[0], new_theta)
        new_chi2 = np.sum(np.square((data[1] - new_calc_y) / data[2]))
        prob = np.exp((-new_chi2 + chi2) / 2)
        n = np.random.rand()
        if n < prob:
            i += 1
            theta = new_theta
            chi2 = new_chi2
        if i > nburn:
            accepted = np.append(accepted, theta)
            accepted = np.reshape(
                accepted, (i - nburn, theta.size)
            )
    return accepted
```


and y_{exp} is the experimental data, and $\text{d}y_{\text{exp}}$ the uncertainty in the experimental data, while y_{calc} is the model solution. Some random perturbation is then applied to the optimised solution,

$$\Theta = \theta + aR, \quad (2.61)$$

where $R \sim N(0, 1)$ and a is the step size. A new χ^2 is found for Θ , and the probability that this transition will occur is found,

$$p = \exp\left(\frac{-\chi^2(\Theta) + \chi^2(\theta)}{2}\right). \quad (2.62)$$

This probability is then compared with a random number $n \sim U[0, 1)$, and if n is less than the probability, the new solution is stored,

$$\theta \leftarrow \Theta. \quad (2.63)$$

This process is repeated until some desired number of samples has been obtained. It should be noted that in the event on a poorly optimised initial value of θ , it may be necessary to ‘burn’¹¹⁴ the first series of solutions while the MCMC algorithm settles into the search-space.

¹¹⁴ This means to ignore.

2.4.4 Molecular dynamics

Section 2.3 introduced classical potential models as a method for the evaluation of the interaction energy of a given chemical system. Any of the optimisation methods discussed above could be used alongside these classical potential models to find an energy minimum structure for the system or to sample the potential energy landscape. However, it is often the case that we are interested in a dynamically relevant structure at a given temperature for some system. This is where molecular dynamics simulations are a useful and important tool.

The aim of a molecular dynamics simulation is to probe the positions, velocities, and accelerations on each of the atoms, or coarse-grained particles, as a simulation progresses. The acceleration on a given particle, \mathbf{a} is defined by the force on that particle, \mathbf{f} , in agreement with Newton’s second law of motion,

$$\mathbf{f} = m\mathbf{a}, \quad (2.64)$$

where, m is the mass of the particle. In order to determine the acceleration on the particle, it is necessary to know the force on that particle. The force, f , is a function of the potential energy, E , as found from a classical potential, of that atom,

$$f(r) = \frac{-\delta E_{\text{total}}(r)}{\delta r}, \quad (2.65)$$

where, r is the configuration of the atoms. Which is to say that, the force is the negative of the first derivative of the energy with

respect to the atomic configuration. The force found from Equation 2.65 is a scalar, however, we are interested in the force vector in Equation 2.64. To determine the force in a given direction, it is necessary to find the product of the force, f , and the unit vector in that direction,

$$\mathbf{f}_x = f \hat{\mathbf{r}}_x, \quad \text{where } \hat{\mathbf{r}}_x = \frac{r_x}{|\mathbf{r}|}, \quad (2.66)$$

where r_x is the atomic configuration in the x -dimension, and $|\mathbf{r}|$ is the magnitude of the atomic configuration vector.

The potential model, which we define for a given system, allows for the calculation of the acceleration on each particle in that system. The next step is to use this acceleration to iterate through the trajectory of our system. This is achieved by applying Newtonian equations of motion, for example in the Velocity-Verlet algorithm.¹¹⁵

¹¹⁵ W. C. Swope *et al.* *J. Chem. Phys.* 76.1 (1982), pp. 637–649.

$$\mathbf{x}(t + \Delta t) = \mathbf{x}(t) + \mathbf{v}(t)\Delta t + \frac{1}{2}\mathbf{a}(t)\Delta t^2, \quad (2.67)$$

$$\mathbf{v}(t + \Delta t) = \mathbf{v}(t) + \frac{1}{2}[\mathbf{a}(t) + \mathbf{a}(t + \Delta t)]\Delta t, \quad (2.68)$$

where, \mathbf{x} is the position the particle \mathbf{v} is the particle's velocity, and \mathbf{a} is the particle's acceleration, while t is current simulation time and Δt is the timestep. These equations constitute the Velocity-Verlet algorithm,

1. calculate the force (and therefore the acceleration) on each particle (Equations 2.64 & 2.65),
2. find the position of the particle after some timestep (Equation 2.67),
3. determine the new velocity for each particle, based on the average acceleration at the current and new positions (Equation 2.68),
4. overwrite the old acceleration values with the new ones,
5. go to 1.

Following an equilibration period, this algorithm may be iterated as many times as is required to obtain sufficient statistics for the measurement quantity of interest, e.g. particle positions for structural techniques such as elastic scattering.

The above analytical process is known as the integration step, and the Velocity-Verlet is the integrator. If the size of the timestep Δt is too large, the step size for a given iteration will not be accurate, as the forces on the atoms will change too significantly during it. Therefore, the values of the timestep is usually on the order of 10×10^{-15} s (fs). This means that in order to simulate a single nanosecond of “real-time” molecular dynamics, the integrator must be solved one million times. This can be slow for very large

systems, leading to an interest in coarse-grained simulations that result in fewer particles to determine the forces for (speeding up the integration step), but also enable to use of larger timesteps (so fewer integrations must be solved),¹¹⁶ for example, the use of a MARTINI potential model allows for an upto twenty times increase in the timestep compared to an all-atom model.

The above discussion ignored two aspects that are necessary to run a molecular dynamics simulation, both of which are associated with the original configuration of the system; the original particle positions and velocities.

The particle positions are usually taken from some library, for example for the simulation of a protein, often the protein data bank¹¹⁷ is a useful resource. Small molecules may be configured by hand using graphical programs such as Jmol.¹¹⁸ These small molecules may be built into complex, multicomponent structures using software such as the Packmol package.¹¹⁹ The importance of this initial structure cannot be overstated, for example, if the initial structure in a molecular dynamics simulation is unrepresentative of the equilibrium structure, it may take a large amount of simulation time before the equilibrium structure is obtained, possibly much longer than could be reasonably simulated.

The initial particle velocities are obtained in a much more general fashion. They are selected randomly, and then scaled such that the kinetic energy, E_k , of the system agrees with a defined temperature, T ,

$$E_k = \sum_{i=1}^N \frac{m_i |\mathbf{v}_i|^2}{2} = \frac{3}{2} N k_B T, \quad (2.69)$$

where, m_i and \mathbf{v}_i are the masses and velocities of the particles, N is the number of particles, and k_B is the Boltzmann constant.

The above algorithm details a simulation that makes use of an NVE ensemble, a simulation where the number of particles (N), the volume of the system (V), the energy of the system (E) are all kept constant. However, this is not the only simulation ensemble that is available, within this work two other ensembles have been used extensively,

- the NVT (canonical) ensemble; this is similar to the NVE ensemble except the simulation temperature is controlled via a thermostat,
- the NPT (isothermal-isobaric); this ensemble is similar to the NVT ensemble, however, the system volume is allowed to vary while the overall system pressure is held constant using a barostat.

Thermostating involves controlling the kinetic energy of the particles (Equation 2.69) such that the simulation temperature is kept at a predefined value. There are a variety of methods for thermostat-

¹¹⁶ R. E. Rudd *et al.* *Phys. Rev. B* 58.10 (1998), R5893–R5896; E. Brini *et al.* *Soft Matter* 9.7 (2013), pp. 2108–2119.

¹¹⁷ *RCSB PDB: Protein Data Bank.* URL: <http://www.rcsb.org> (Accessed 2018-1-28).

¹¹⁸ *Jmol: An Open-Source Java Viewer for Chemical Structures in 3D.* URL: <http://www.jmol.org/> (Accessed 2018-1-28).

¹¹⁹ L. Martínez *et al.* *J. Comput. Chem.* 30.13 (2009), pp. 2157–2164.

¹²⁰ H. C. Andersen. *J. Chem. Phys.* 72.4 (1980), pp. 2384–2393; S. Nosé. *J. Chem. Phys.* 81.1 (1984), pp. 511–519; H. J. C. Berendsen *et al.* *J. Chem. Phys.* 81.8 (1984), pp. 3684–3690; W. G. Hoover. *Phys. Rev. A* 31.3 (1985), pp. 1695–1697.

¹²¹ A. R. McCluskey *et al.* *J. Open Source Educ.* 1.2 (2018), pp. 19–21; A. R. McCluskey *et al.* *Arm61/PyJl: PyJl-1.1.0*. 2018. URL: <http://doi.org/10.5281/zenodo.1403828>.

¹²² G. Bussi *et al.* *J. Chem. Phys.* 126.1 (2007), p. 014101.

¹²³ M. Parrinello *et al.* *J. Appl. Phys.* 52.12 (1981), pp. 7182–7190.

ing a molecular dynamics simulation, such as the Andersen, Nosé-Hoover, or Berendsen methods.¹²⁰ However, the most straightforward to describe, and that implemented in the `pylj` software (discussed in detail in Chapter ??)¹²¹ is a velocity rescaling.¹²² This is where the velocities for a random subset of the particles, \mathbf{v}_i are adapted based on the following relation,

$$\mathbf{v}_i \leftarrow \mathbf{v}_i \sqrt{\frac{T_{\text{target}}}{\bar{T}}} \quad (2.70)$$

where, T_{target} is the target temperature, and \bar{T} is the average simulation temperature.

The use of a barostat to control the simulation pressure usually involves varying the simulation cell parameters and the distances between the particles. This would in a similar way to thermostating, where the simulation dimensions are scaled by a value in an effort to control the pressure. The barostating methods are similar to the thermostating methods with Andersen, Nosé-Hoover, and Berendsen methods. However, there is also the Parrinello-Rahman barostat which allows for independent control of the different cell dimensions giving control of stress in addition to pressure.¹²³

These optimisation and sampling methods were used in a variety of different applications within this work, firstly differential evolution optimisation and MCMC sampling are used in Chapter ?? in the study of a chemically-consistent modelling approach to X-ray and neutron reflectometry analysis. Molecular dynamics simulation are investigated as a possible tool to assist in the analysis of reflectometry in Chapter ?. Finally, the particle swarm optimisation is applied for the efficient determination of a micelle structure for fitting small angle scattering data in Chapter ?.

A

ADDITIONAL CODE BLOCKS FOR DIFFERENTIAL EVOLUTION

```
import numpy as np

def mutation(p, b, km):
    """
    Performs the mutation step, where the parent population vector
    is transformed to produce a mutant vector.

    Parameters
    -----
    p: float, array_like
        The parent population vector. An array of shape (i, j),
        where i is the number of variables and j is the population
        size.
    b: float, array_like
        The best member of the parent population. An array of
        size i, where i is the number of variables.
    km: float
        The mutation constant.

    Returns
    -----
    float, array_like
        The mutant vector. An array of shape (i, j), where i is
        the number of variables and j is the population size.
    """
    m = np.zeros_like(p)
    R = np.random.randint(p.shape[1], size=(2, p.shape[1]))
    for j in range(p.shape[1]):
        m[:, j] = b + km * (p[:, R[0, j]] - p[:, R[1, j]])
    return m
```

Code Block A.1: The mutation step used in a classical trial method for a differential evolution algorithm, as described in M. Björck. *J. Appl. Crystallogr.* 44.6 (2011), pp. 1198–1204.

```
import numpy as np

def recombination(p, m, kr):
    """
    The recombination step, where the mutant and parent population
    vectors are combined.

    Parameters
    -----
    p: float, array_like
        The parent population vector. An array of shape (i, j),
        where i is the number of variables and j is the population
        size.
    m: float, array_like
        The mutant vector. An array of shape (i, j), where i
        is the number of variables and j is the population size.
    kr: float
        The recombination constant.

    Returns
    -----
    float, array_like
        The offspring population vector. An array of shape (i, j),
        where i is the number of variables and j is the population
        size.
    """
    o = np.array(p)
    rand = np.random.rand(p.shape[0], p.shape[1])
    o[rand < kr] = m[rand < kr]
    return o
```

Code Block A.2: The recombination step used in a classical trial method for a differential evolution algorithm, as described in M. Björck. *J. Appl. Crystallogr.* 44.6 (2011), pp. 1198–1204.

```

import numpy as np

def selection(p, o, f):
    """
    The selection function, where the population member that
    return the minimum value for the figure of merit is brought
    forward to the next generation.

    Parameters
    -----
    p: float, array_like
        The parent population vector. An array of shape (i, j),
        where i is the number of variables and j is the population
        size.
    o: float, array_like
        The offspring population vector. An array of shape (i, j),
        where i is the number of variables and j is the population
        size.
    f: function
        The figure of merit function to be minimised.

    Returns
    -----
    float, array_like
        The new parent population vector. An array of shape (i, j),
        where i is the number of variables and j is the population
        size.
    """
    new_p = np.array(p)
    for j in range(p.shape[1]):
        p_fom = f(p[:, j])
        o_fom = f(o[:, j])
        if o_fom < p_fom:
            new_p[:, j] = o[:, j]
    return new_p

```

Code Block A.3: The selection step used in a differential evolution algorithm, as described in M. Björck. *J. Appl. Crystallogr.* 44.6 (2011), pp. 1198–1204.

REFERENCES

- Abelès, F. "Sur La Propagation Des Ondes Électromagnétiques Dans Les Milieux Stratifiés". *Ann. Phys.* 12.3 (1948), pp. 504–520. DOI: 10.1051/anphys/194812030504.
- Ackley, D. H. "A Connectionist Machine for Genetic Hillclimbing". PhD. Michigan, US: University of Michigan, 1987. 260 pp.
- Albrecht, O., H. Gruler, and E. Sackmann. "Polymorphism of Phospholipid Monolayers". *J. Phys. France* 39.3 (1978), pp. 301–313. DOI: 10.1051/jphys:01978003903030100.
- Andersen, H. C. "Molecular Dynamics Simulations at Constant Pressure and/or Temperature". *J. Chem. Phys.* 72.4 (1980), pp. 2384–2393. DOI: 10.1063/1.439486.
- Anderson, P. M. and M. R. Wilson. "Molecular Dynamics Simulations of Amphiphilic Graft Copolymer Molecules at a Water/Air Interface". *J. Chem. Phys.* 121.17 (2004), p. 8503. DOI: 10.1063/1.1796251.
- Anton, N., H. Mojziso, E. Porcher, J.-P. Benoit, and P. Saulnier. "Reverse Micelle-Loaded Lipid Nano-Emulsions: New Technology for Nano-Encapsulation of Hydrophilic Materials". *Int. J. Pharm.* 398.1-2 (2010), pp. 204–209. DOI: 10.1016/j.ijpharm.2010.07.039.
- Banks, J. L., H. S. Beard, Y. Cao, A. E. Cho, Wolfgang Damm, R. Farid, A. K. Felts, T. A. Halgren, D. T. Mainz, J. R. Maple, R. Murphy, D. M. Philipp, M. P. Repasky, L. Y. Zhang, B. J. Berne, R. A. Friesner, E. Gallicchio, and R. M. Levy. "Integrated Modeling Program, Applied Chemical Theory (IMPACT)". *J. Comput. Chem.* 26.16 (2005), pp. 1752–1780. DOI: 10.1002/jcc.20292.
- Berendsen, H. J. C., J. P. M. Postma, W. F. van Gunsteren, A. DiNola, and J. R. Haak. "Molecular Dynamics with Coupling to an External Bath". *J. Chem. Phys.* 81.8 (1984), pp. 3684–3690. DOI: 10.1063/1.448118.
- Björck, M. "Fitting with Differential Evolution: An Introduction and Evaluation". *J. Appl. Crystallogr.* 44.6 (2011), pp. 1198–1204. DOI: 10.1107/S0021889811041446.
- Björck, M. and G. Andersson. "GenX: An Extensible X-Ray Reflectivity Refinement Program Utilizing Differential Evolution". *J. Appl. Crystallogr.* 40.6 (2007), pp. 1174–1178. DOI: 10.1107/S0021889807045086.

- Bowerman, S., A. S. J. B. Rana, A. Rice, G. H. Pham, E. R. Strieter, and J. Wereszczynski. "Determining Atomistic SAXS Models of Tri-Ubiquitin Chains from Bayesian Analysis of Accelerated Molecular Dynamics Simulations". *J. Chem. Theory Comput.* 13.6 (2017), pp. 2418–2429. DOI: 10.1021/acs.jctc.7b00059.
- Brini, E., E. A. Algaer, P. Ganguly, C. Li, F. Rodríguez-Ropero, and N. F. A. van der Vegt. "Systematic Coarse-Graining Methods for Soft Matter Simulations – a Review". *Soft Matter* 9.7 (2013), pp. 2108–2119. DOI: 10.1039/C2SM27201F.
- Buckingham, R. A. "The Classical Equation of State of Gaseous Helium, Neon and Argon". *Proc. Royal Soc. Lond. A.* 168.933 (1938), pp. 264–283. DOI: 10.1098/rspa.1938.0173.
- Bussi, G., D. Donadio, and M. Parrinello. "Canonical Sampling through Velocity Rescaling". *J. Chem. Phys.* 126.1 (2007), p. 014101. DOI: 10.1063/1.2408420.
- Campbell, R. A., Y. Saaka, Y. Shao, Y. Gerelli, R. Cubitt, E. Nazaruk, D. Matyszevska, and M. J. Lawrence. "Structure of Surfactant and Phospholipid Monolayers at the Air/Water Interface Modeled from Neutron Reflectivity Data". *J. Colloid Interface Sci.* 531 (2018), pp. 98–108. DOI: 10.1016/j.jcis.2018.07.022.
- Cordobés, F., J. Muñoz, and C. Gallegos. "Linear Viscoelasticity of the Direct Hexagonal Liquid Crystalline Phase for a Heptane/Nonionic Surfactant/Water System". *J. Colloid Interface Sci.* 187.2 (1997), pp. 401–417. DOI: 10.1006/jcis.1996.4707.
- Coulomb, C. A. "Premier Mémoire Sur l'électricité et Le Magnétisme". *Histoire de l'Académie Royale des Sciences*. Imprimerie Royale (1788), pp. 569–577.
- Coulomb, C. A. "Second Mémoire Sur l'électricité et Le Magnétisme". *Histoire de l'Académie Royale des Sciences*. Imprimerie Royale (1788), pp. 578–611.
- Dabkowska, A. P., L. E. Collins, D. J. Barlow, R. Barker, S. E. McLain, M. J. Lawrence, and C. D. Lorenz. "Modulation of Dipalmitoylphosphatidylcholine Monolayers by Dimethyl Sulfoxide". *Langmuir* 30.29 (2014), pp. 8803–8811. DOI: 10.1021/la501275h.
- De Broglie, L. "Recherches Sur La Théorie Des Quanta". *Ann. Phys. (Paris)* 10.3 (1925), pp. 22–125.
- Debye, P. "Zerstreuung von Röntgenstrahlen". *Ann. Phys.* 351.6 (1915), pp. 809–823. DOI: 10.1002/andp.19153510606.
- Edler, K. J. and D. T. Bowron. "Combining Wide-Angle and Small-Angle Scattering to Study Colloids and Self-Assembly". *Curr. Opin. Colloid Interface Sci.* 20.4 (2015), pp. 227–234. DOI: 10.1016/j.cocis.2015.07.002.
- Essmann, U., L. Perera, M. L. Berkowitz, T. Darden, H. Lee, and L. G. Pedersen. "A Smooth Particle Mesh Ewald Method". *J. Chem. Phys.* 103.19 (1995), pp. 8577–8593. DOI: 10.1063/1.470117.

- Ewald, P. P. "Die Berechnung Optischer Und Elektrostatischer Gitterpotentiale". *Ann. Phys.* 369.3 (1921), pp. 253–287. DOI: 10.1002/andp.19213690304.
- Farago, B. "Recent Developments and Applications of NSE in Soft Matter". *Curr. Opin. Colloid Interface Sci.* 14.6 (2009), pp. 391–395. DOI: 10.1016/j.cocis.2009.07.004.
- Foglia, F., M. J. Lawrence, and D. J. Barlow. "Studies of Model Biological and Bio-Mimetic Membrane Structure: Reflectivity vs Diffraction, a Critical Comparison". *Curr. Opin. Colloid Interface Sci.* 20.4 (2015), pp. 235–243. DOI: 10.1016/j.cocis.2015.08.001.
- Frenkel, D. and B. Smit. *Understanding Molecular Simulation: From Algorithms to Applications*. San Diego, USA: Academic Press, 1996. ISBN: 978-0-12-267351-1.
- Garcia Sakai, V. and A. Arbe. "Quasielastic Neutron Scattering in Soft Matter". *Curr. Opin. Colloid Interface Sci.* 14.6 (2009), pp. 381–390. DOI: 10.1016/j.cocis.2009.04.002.
- Garcia-Gutierrez, M. C. and D. R. Rueda. "Bases of Synchrotron Radiation, Light Sources, and Features of X-Ray Scattering Beamlines". In: *Applications of Synchrotron Light to Scattering and Diffraction in Materials and Life Sciences*. Ed. by M. Gomez, A. Nogales, M. C. Garcia-Gutierrez, and T. A. Ezquerra. Berlin, DE: Springer-Verlag Berlin Heidelberg, 2009, pp. 1–22. ISBN: 978-3-540-95968-7.
- Gerelli, Y. "Aurore: New Software for Neutron Reflectivity Data Analysis". *J. Appl. Crystallogr.* 49.1 (2016), pp. 330–339. DOI: 10.1107/S1600576716000108.
- Gerelli, Y. "Aurore: New Software for Neutron Reflectivity Data Analysis. Corrigendum". *J. Appl. Crystallogr.* 49.2 (2016), pp. 712–712. DOI: 10.1107/S1600576716002466.
- Gilks, W., S. Richardson, and D. Spiegelhalter. *Markov Chain Monte Carlo in Practice*. Chapman & Hall/CRC Interdisciplinary Statistics. Boca Raton, US: CRC Press, 1995. ISBN: 978-0-412-05551-5.
- Goodwin, J. *Colloids and Interfaces with Surfactants and Polymers*. 2nd ed. Chichester, UK: John Wiley & Sons, 2009. ISBN: 978-0-470-51880-9.
- Grillo, I. "Small-Angle Neutron Scattering and Applications in Soft Condensed Matter". In: *Soft-Matter Characterization*. Ed. by R. Borsali and R. Pecora. New York, USA: Springer, 2008, pp. 723–782. ISBN: 978-1-4020-4465-6.
- Gumbart, J., L. G. Trabuco, E. Schreiner, E. Villa, and K. Schulten. "Regulation of the Protein-Conducting Channel by a Bound Ribosome". *Structure* 17.11 (2009), pp. 1453–1464. DOI: 10.1016/j.str.2009.09.010.
- Hargreaves, R., D. T. Bowron, and K. Edler. "Atomistic Structure of a Micelle in Solution Determined by Wide Q -Range Neutron Diffraction". *J. Am. Chem. Soc.* 133.41 (2011), pp. 16524–16536. DOI: 10.1021/ja205804k.

- Harvey, J. *Computational Chemistry*. Oxford: Oxford University Press, 2018. ISBN: 978-0-19-875550-0.
- Hassan, P. A., G. Fritz, and E. W. Kaler. "Small Angle Neutron Scattering Study of Sodium Dodecyl Sulfate Micellar Growth Driven by Addition of a Hydrotropic Salt". *J. Colloid Interface Sci.* 257.1 (2003), pp. 154–162. DOI: 10.1016/S0021-9797(02)00020-6.
- Hastings, W. K. "Monte Carlo Sampling Methods Using Markov Chains and Their Applications". *Biometrika* 57.1 (1970), pp. 97–109. DOI: 10.1093/biomet/57.1.97.
- Hayter, J. B. and J. Penfold. "An Analytic Structure Factor for Macroion Solutions". *Mol. Phys.* 42.1 (1981), pp. 109–118. DOI: 10.1080/00268978100100091.
- Hayward, D. W., J. B. Gilroy, P. A. Rupar, L. Chabanne, C. Pizzey, M. A. Winnik, G. R. Whittell, I. Manners, and R. M. Richardson. "Liquid Crystalline Phase Behavior of Well-Defined Cylindrical Block Copolymer Micelles Using Synchrotron Small-Angle X-Ray Scattering". *Macromolecules* 48.5 (2015), pp. 1579–1591. DOI: 10.1021/ma502222f.
- Hazell, G., A. P. Gee, T. Arnold, K. J. Edler, and S. E. Lewis. "Langmuir Monolayers Composed of Single and Double Tail Sulfobetaine Lipids". *J. Colloid Interface Sci.* 474 (2016), pp. 190–198. DOI: 10.1016/j.jcis.2016.04.020.
- Holland, J. H. *Adaptation in Natural and Artificial Systems*. 2nd ed. Boston, USA: MIT Press, 1992. ISBN: 978-0-262-58111-0.
- Hoover, W. G. "Canonical Dynamics: Equilibrium Phase-Space Distributions". *Phys. Rev. A* 31.3 (1985), pp. 1695–1697. DOI: 10.1103/PhysRevA.31.1695.
- Hub, J. S. "Interpreting Solution X-Ray Scattering Data Using Molecular Simulations". *Curr. Opin. Struct. Biol.* 49 (2018), pp. 18–26. DOI: 10.1016/j.sbi.2017.11.002.
- Hughes, A. V. *RasCAL*. URL: <https://sourceforge.net/projects/rscl/> (Accessed 2016-8-8).
- Humphrey, W., A. Dalke, and K. Schulten. "VMD: Visual Molecular Dynamics". *J. Mol. Graph.* 14.1 (1996), pp. 33–38. DOI: 10.1016/0263-7855(96)00018-5.
- ILL: *Neutron for Science: Technical Characteristics*. URL: <https://www.ill.eu/reactor-environment-safety/high-flux-reactor/technical-characteristics/> (Accessed 2016-8-8).
- ISIS – *How ISIS Works*. URL: <https://www.isis.stfc.ac.uk/Pages/What-does-ISIS-Neutron-Muon-Source-do.aspx> (Accessed 2018-9-25).
- ISIS – *SANS2D*. URL: <https://www.isis.stfc.ac.uk/Pages/Sans2d.aspx> (Accessed 2018-9-25).
- Israelachvili, J. *Intermolecular and Surface Forces*. 3rd ed. Cambridge, USA: Academic Press, 2011. ISBN: 978-0-12-391933-5.

- Ivanović, M. T., L. K. Bruetzel, J. Lipfert, and J. S. Hub. "Temperature-Dependent Atomic Models of Detergent Micelles Refined against Small-Angle X-Ray Scattering Data". *Angew. Chemie Int. Ed.* 57.20 (2018), pp. 5635–5639. DOI: 10.1002/anie.201713303.
- Jensen, G. V., R. Lund, J. Gummel, T. Narayanan, and J. S. Pedersen. "Monitoring the Transition from Spherical to Polymer-like Surfactant Micelles Using Small-Angle X-Ray Scattering". *Angew. Chemie Int. Ed.* 53.43 (2014), pp. 11524–11528. DOI: 10.1002/anie.201406489.
- Jmol: An Open-Source Java Viewer for Chemical Structures in 3D. URL: <http://www.jmol.org/> (Accessed 2018-1-28).
- Jones, R. A. L. *Soft Condensed Matter*. Oxford, UK: Oxford University Press, 2002. ISBN: 978-0-19-850589-1.
- Jorgensen, W. L. and J. Tirado-Rives. "The OPLS [Optimized Potentials for Liquid Simulations] Potential Functions for Proteins, Energy Minimizations for Crystals of Cyclic Peptides and Crambin". *J. Am. Chem. Soc.* 110.6 (1988), pp. 1657–1666. DOI: 10.1021/ja00214a001.
- Jurašin, D., M. Vinceković, A. Pustak, I. Šmit, M. Bujan, and N. Filipović-Vinceković. "Lamellar to Hexagonal Columnar Liquid Crystalline Phase Transition in a Catanionic Surfactant Mixture: Dodecylammonium Chloride–Sodium Bis(2-Ethylhexyl) Sulfosuccinate". *Soft Matter* 9.12 (2013), p. 3349. DOI: 10.1039/c3sm27665a.
- Kataoka, K., A. Harada, and Y. Nagasaki. "Block Copolymer Micelles for Drug Delivery: Design, Characterization and Biological Significance". *Adv. Drug Deliv. Rev.* 64 (2012), pp. 37–48. DOI: 10.1016/j.addr.2012.09.013.
- Kennedy, J. and R. Eberhart. "Particle Swarm Optimization". In: *Proceedings of ICNN'95. International Conference on Neural Networks*. Perth, AU: IEEE, 1995, pp. 1942–1948. DOI: 10.1109/ICNN.1995.488968.
- Kewalramani, S., H. Hlaing, B. M. Ocko, I. Kuzmenko, and M. Fukuto. "Effects of Divalent Cations on Phase Behavior and Structure of a Zwitterionic Phospholipid (DMPC) Monolayer at the Air–Water Interface". *J. Phys. Chem. Lett.* 1.2 (2010), pp. 489–495. DOI: 10.1021/jz9002873.
- Kienzle, P. A., M. Douchet, D. J. McGilivray, K. V. O'Donovan, N. K. Berk, and C. F. Majkrzak. *NCNR Reflectometry Software*. URL: <http://www.ncnr.nist.gov/reflpak> (Accessed 2018-3-4).
- Klein, R. "Interacting Colloidal Suspensions". In: *Neutron, X-Rays and Light. Scattering Methods Applied to Soft Condensed Matter*. Ed. by Th. Zemb and P. Lindner. Amsterdam, NL: Elsevier Science B.V., 2002, pp. 351–380. ISBN: 978-0-08-093013-8.
- Kmiecik, S., D. Gront, M. Kolinski, L. Wieteska, A. E. Dawid, and A. Kolinski. "Coarse-Grained Protein Models and Their Applications". *Chem. Rev.* 116.14 (2016), pp. 7898–7936. DOI: 10.1021/acs.chemrev.6b00163.

- Koutsoubas, A. "Combined Coarse-Grained Molecular Dynamics and Neutron Reflectivity Characterization of Supported Lipid Membranes". *J. Phys. Chem. B* 120.44 (2016), pp. 11474–11483. DOI: 10.1021/acs.jpcc.6b05433.
- Kraft, D. J., J. Hilhorst, M. A. P. Heinen, M. J. Hoogenraad, B. Luigjes, and W. K. Kegel. "Patchy Polymer Colloids with Tunable Anisotropy Dimensions". *J. Phys. Chem. B* 115.22 (2011), pp. 7175–7181. DOI: 10.1021/jp108760g.
- Kratky, O and G Porod. "Diffuse Small-Angle Scattering of x-Rays in Colloid Systems". *J. Colloid Sci.* 4.1 (1949), pp. 35–70. DOI: 10.1016/0095-8522(49)90032-X.
- Krauth, W. *Statistical Mechanics: Algorithms and Computations*. Oxford Master Series in Statistical, Computational, and Theoretical Physics 13. Oxford, UK: Oxford University Press, 2006. ISBN: 978-0-19-851536-4.
- Leach, A. R. *Molecular Modelling: Principles and Applications*. Harlow, UK: Addison Wesley London Ltd, 1996. ISBN: 978-0-582-38210-7.
- Lennard-Jones, J. E. "On the Determination of Molecular Fields. II. From the Equation of State of a Gas". *Proc. Royal Soc. Lond. A*. 106.738 (1924), pp. 463–477. DOI: 10.1098/rspa.1924.0082.
- Levenberg, K. "A Method for the Solution of Certain Non-Linear Problems in Least Squares". *Quart. Appl. Math.* 2.2 (1944), pp. 164–168. DOI: 10.1090/qam/10666.
- Lu, J. R., E. M. Lee, and R. K. Thomas. "The Analysis and Interpretation of Neutron and X-Ray Specular Reflection". *Acta Crystallogr. A* 52.1 (1996), pp. 11–41. DOI: 10.1107/S0108767395011202.
- Marquardt, D. W. "An Algorithm for Least-Squares Estimation of Nonlinear Parameters". *J. Soc. Indust. Appl. Math.* 11.2 (1963), pp. 431–441. DOI: 10.1137/0111030.
- Marrink, S. J., H. J. Risselada, S. Yefimov, D. P. Tieleman, and A. H. de Vries. "The MARTINI Force Field: Coarse Grained Model for Biomolecular Simulations". *J. Phys. Chem. B* 111.27 (2007), pp. 7812–7824. DOI: 10.1021/jp071097f.
- Martínez, L., R. Andrade, E. G. Birgin, and J. M. Martínez. "PACKMOL: A Package for Building Initial Configurations for Molecular Dynamics Simulations". *J. Comput. Chem.* 30.13 (2009), pp. 2157–2164. DOI: 10.1002/jcc.21224.
- McCluskey, A. R. and K. J. Edler. "Model-Dependent Small-Angle Scattering for the Study of Complex Organic Materials". *Curr. Org. Chem.* 22.8 (2018), pp. 750–757. DOI: 10.2174/1875692115666170612104439.
- McCluskey, A. R., B. J. Morgan, K. J. Edler, and S. C. Parker. *Arm61/PyIj: PyIj-1.1.0*. 2018. URL: <http://doi.org/10.5281/zenodo.1403828>.
- McCluskey, A. R., B. J. Morgan, K. J. Edler, and S. C. Parker. "PyIj: A Teaching Tool for Classical Atomistic Simulation". *J. Open Source Educ.* 1.2 (2018), pp. 19–21. DOI: 10.21105/jose.00019.

- MetalJet X-Ray Source Technology*. URL: <https://www.excillum.com/technology/> (Accessed 2018-12-6).
- Metropolis, N., A.W. Rosenbluth, M. N. Rosenbluth, A. H. Teller, and E. Teller. "Equation of State Calculations by Fast Computing Machines". *J. Chem. Phys.* 21.6 (1953), pp. 1087–1092. DOI: 10.1063/1.1699114.
- Miller, A. F., M. R. Wilson, M. J. Cook, and R. W. Richards. "Monte Carlo Simulations of an Amphiphilic Polymer at a Hydrophobic/Hydrophilic Interface". *Mol. Phys.* 101.8 (2003), pp. 1131–1138. DOI: 10.1080/0026897031000068569.
- Mohwald, H. "Phospholipid and Phospholipid-Protein Monolayers at the Air-Water Interface". *Annu. Rev. Phys. Chem.* 41 (1990), pp. 441–476. DOI: 10.1146/annurev.pc.41.100190.002301.
- Morse, P. M. "Diatomic Molecules According to the Wave Mechanics. II. Vibrational Levels". *Phys. Rev.* 34.1 (1929), pp. 57–64. DOI: 10.1103/PhysRev.34.57.
- Nelson, A. R. J. "Co-Refinement of Multiple-Contrast Neutron/X-Ray Reflectivity Data Using MOTOFIT". *J. Appl. Crystallogr.* 39.2 (2006), pp. 273–276. DOI: 10.1107/S0021889806005073.
- Nelson, A. R. J. "Towards a Detailed Resolution Smearing Kernel for Time-of-Flight Neutron Reflectometers. Corrigendum". *J. Appl. Crystallogr.* 47.3 (2014), p. 1162. DOI: 10.1107/S1600576714009595.
- Nelson, A. R. J. and C. D. Dewhurst. "Towards a Detailed Resolution Smearing Kernel for Time-of-Flight Neutron Reflectometers". *J. Appl. Crystallogr.* 46.5 (2013), pp. 1338–1346. DOI: 10.1107/S0021889813021936.
- Nelson, A. R. J. and S. W. Prescott. "Refnx: Neutron and X-Ray Reflectometry Analysis in Python". *J. Appl. Crystallogr.* 52.1 (2019), pp. 193–200. DOI: 10.1107/S1600576718017296.
- Nénot, L. and P. Croce. "Caractérisation Des Surfaces Par Réflexion Rasante de Rayons X. Application à l'étude Du Polissage de Quelques Verres Silicates". *Rev. Phys. Appl. (Paris)* 15.3 (1980), pp. 761–779. DOI: 10.1051/rphysap:01980001503076100.
- Nosé, S. "A Unified Formulation of the Constant Temperature Molecular Dynamics Methods". *J. Chem. Phys.* 81.1 (1984), pp. 511–519. DOI: 10.1063/1.447334.
- Ott, F. *SimulReflec*. URL: <http://www-llb.cea.fr/prism/programs/simulreflec/simulreflec.html> (Accessed 2019-3-4).
- Pambou, E., J. Crewe, M. Yaseen, F. N. Padia, S. Rogers, D. Wang, H. Xu, and J. R. Lu. "Structural Features of Micelles of Zwitterionic Dodecyl-Phosphocholine (C₁₂ PC) Surfactants Studied by Small-Angle Neutron Scattering". *Langmuir* 31.36 (2015), pp. 9781–9789. DOI: 10.1021/acs.langmuir.5b02077.
- Parratt, L. G. "Surface Studies of Solids by Total Reflection of X-Rays". *Phys. Rev.* 95.2 (1954), pp. 359–369. DOI: 10.1103/PhysRev.95.359.

- Parrinello, M. and A. Rahman. "Polymorphic Transitions in Single Crystals: A New Molecular Dynamics Method". *J. Appl. Phys.* 52.12 (1981), pp. 7182–7190. DOI: 10.1063/1.328693.
- Pedersen, J. S. "Monte Carlo Simulation Techniques Applied in the Analysis of Small-Angle Scattering Data from Colloids and Polymer System". In: *Neutron, X-Rays and Light. Scattering Methods Applied to Soft Condensed Matter*. Ed. by Th. Zemb and P. Lindner. Amsterdam, NL: Elsevier Science B.V., 2002, pp. 381–390. ISBN: 978-0-08-093013-8.
- Pluhackova, K. and R. A. Böckmann. "Biomembranes in Atomistic and Coarse-Grained Simulations". *J. Phys. Condens. Matter* 27.32 (2015), p. 323103. DOI: 10.1088/0953-8984/27/32/323103.
- Poli, R. "Analysis of the Publications on the Applications of Particle Swarm Optimisation". *J. Artif. Evol. Appl.* 2008 (2008), pp. 1–10. DOI: 10.1155/2008/685175.
- Rahman, A. "Correlations in the Motion of Atoms in Liquid Argon". *Phys. Rev.* 136 (2A 1964), A405–A411. DOI: 10.1103/PhysRev.136.A405.
- RCSB PDB: Protein Data Bank. URL: <http://www.rcsb.org> (Accessed 2018-1-28).
- Rodriguez-Loureiro, I., E. Scoppola, L. Bertinetti, A. Barbeta, G. Fragneto, and E. Schneck. "Neutron Reflectometry Yields Distance-Dependent Structures of Nanometric Polymer Brushes Interacting across Water". *Soft Matter* 13.34 (2017), pp. 5767–5777. DOI: 10.1039/C7SM01066D.
- Rondelli, V., G. Fragneto, S. S., E. Del Favero, and L. Cantù. "Reflectivity from Floating Bilayers: Can We Keep the Structural Asymmetry?" *J. Phys. Conf. Ser.* 340 (2012), p. 012083. DOI: 10.1088/1742-6596/340/1/012083.
- Rose, D. R., J. Phipps, J. Michniewicz, G. I. Birnbaum, F. R. Ahmed, A. Muir, W. F. Anderson, and S. Narang. "Crystal Structure of T4-Lysozyme Generated from Synthetic Coding DNA Expressed in Escherichia Coli". *Protein Eng. Des. Sel.* 2.4 (1988), pp. 277–282. DOI: 10.1093/protein/2.4.277.
- Rosen, M. J. and J. T. Kunjappu. *Surfactants and Interfacial Phenomena*. 4th ed. Hoboken, USA: John Wiley & Sons, 2012. ISBN: 978-0-470-54194-4.
- Rudd, R. E and J. Q. Broughton. "Coarse-Grained Molecular Dynamics and the Atomic Limit of Finite Elements". *Phys. Rev. B* 58.10 (1998), R5893–R5896. DOI: 10.1103/PhysRevB.58.R5893.
- Sammalkorpi, M., M. Karttunen, and M. Haataja. "Ionic Surfactant Aggregates in Saline Solutions: Sodium Dodecyl Sulfate (SDS) in the Presence of Excess Sodium Chloride (NaCl) or Calcium Chloride (CaCl_2)". *J. Phys. Chem. B* 113.17 (2009), pp. 5863–5870. DOI: 10.1021/jp901228v.
- SASfit. URL: <https://kur.web.psi.ch/sans1/SANSSoft/sasfit.html> (Accessed 2018-11-11).

- SASview for Small Angle Scattering*. URL: <http://www.sasview.org> (Accessed 2016-10-26).
- Schmaljohann, D. "Thermo- and pH-Responsive Polymers in Drug Delivery". *Adv. Drug Deliv. Rev.* 58.15 (2006), pp. 1655–1670. DOI: 10.1016/j.addr.2006.09.020.
- Schnablegger, H. and Y. Singh. *The SAXS Guide: Getting Acquainted with the Principles*. 4th ed. Graz, AT: Anton Paar GmbH, 2017.
- Schramm, L. L., E. N. Stasiuk, and D. G. Marangoni. "Surfactants and Their Applications". *Annu. Rep. Prog. Chem., Sect. C: Phys. Chem.* 99 (2003), pp. 3–48. DOI: 10.1039/B208499F.
- Schurtenberger, P. "Contrast and Contrast Variation in Neutron, x-Ray and Light Scattering". In: *Neutron, X-Rays and Light Scattering Methods Applied to Soft Condensed Matter*. Ed. by Th. Zemb and P. Lindner. Amsterdam, NL: Elsevier Science B.V., 2002, pp. 145–170. ISBN: 978-0-08-093013-8.
- Scoppola, E. and E. Schneck. "Combining Scattering and Computer Simulation for the Study of Biomolecular Soft Interfaces". *Curr. Opin. Colloid Interface Sci.* 37 (2018), pp. 88–100. DOI: 10.1016/j.cocis.2018.06.008.
- Shi, Y. and R. Eberhart. "A Modified Particle Swarm Optimizer". In: *1998 IEEE International Conference on Evolutionary Computation Proceedings*. IEEE World Congress on Computational Intelligence. Anchorage, US: IEEE, 1998, pp. 69–73. DOI: 10.1109/ICEC.1998.699146.
- Simons, K. and D. Toomre. "Lipid Rafts and Signal Transduction". *Nat. Rev. Mol. Cell Biol.* 1 (2000), pp. 31–39. DOI: 10.1038/35036052.
- Sivia, D. S. *Elementary Scattering Theory: For X-Ray and Neutron Users*. Oxford, UK: Oxford University Press, 2011. ISBN: 978-0-19-922868-3.
- Sivia, D. S. and J. Skilling. *Data Analysis: A Bayesian Tutorial*. 2nd ed. Oxford: Oxford University Press, 2006. ISBN: 978-0-19-856832-2.
- Skou, S., R. E. Gillilan, and N. Ando. "Synchrotron-Based Small-Angle X-Ray Scattering of Proteins in Solution". *Nat. Protoc.* 9.7 (2014), pp. 1727–1739. DOI: 10.1038/nprot.2014.116.
- Storn, R. and K. Price. "Differential Evolution – A Simple and Efficient Heuristic for Global Optimization over Continuous Spaces". *J. Global Optim.* 11 (1997), pp. 341–359. DOI: 10.1023/A:1008202821328.
- Svergun, D. I. "Solution Scattering from Biopolymers: Advanced Contrast-Variation Data Analysis". *Acta Crystallogr. A* 50.3 (1994), pp. 391–402. DOI: 10.1107/S0108767393013492.
- Swope, W. C., H. C. Andersen, P. H. Berens, and K. R. Wilson. "A Computer Simulation Method for the Calculation of Equilibrium Constants for the Formation of Physical Clusters of Molecules: Application to Small Water Clusters". *J. Chem. Phys.* 76.1 (1982), pp. 637–649. DOI: 10.1063/1.442716.

- Watson, M. C. and J. E. Curtis. "Rapid and Accurate Calculation of Small-Angle Scattering Profiles Using the Golden Ratio". *J. Appl. Crystallogr.* 46.4 (2013), pp. 1171–1177. DOI: 10.1107/S002188981301666X.
- Willis, B. T. M. and C. J. Carlile. *Experimental Neutron Scattering*. Oxford, UK: Oxford University Press, 2009. ISBN: 978-0-19-967377-3.
- Wormington, M., C. Panaccione, K. M. Matney, and D. K. Bowen. "Characterization of Structures from X-Ray Scattering Data Using Genetic Algorithms". *Philos. Trans. R. Soc. London Ser. A* 357.1761 (1999), pp. 2827–2848. DOI: 10.1098/rsta.1999.0469.
- Wu, G., R. Mallipeddi, and P. N. Suganthan. "Ensemble Strategies for Population-Based Optimization Algorithms – A Survey". *Swarm Evol. Comput.* 44 (2019), pp. 695–711. DOI: 10.1016/j.swevo.2018.08.015.
- Zagnoni, M. "Miniaturised Technologies for the Development of Artificial Lipid Bilayer Systems". *Lab on a Chip* 12.6 (2012), p. 1026. DOI: 10.1039/c2lc20991h.